The Abdus Salam
International Centre for Theoretical Physics

United Nations
Educational, Scientific and
Cultural Organization

IAEA
International Atomic Energy Agency

1965-25

9th Workshop on Three-Dimensional Modelling of Seismic Waves Generation, Propagation and their Inversion

22 September - 4 October, 2008

Upper mantle Anisotropy from Surface Wave studies

Jean-Paul Montagner
Seismological Laboratory
Institut de Physique du Globe
Paris
France

jpm@ipgp.jussieu.fr

Upper mantle Anisotropy from Surface Wave studies

Jean-Paul Montagner[(1)]

[(1)] *Seismological Laboratory, CNRS UMR 7154, Institut de Physique du Globe, Paris, France*

Modified version of the Chapter entitled "Upper mantle Structure: Global isotropic and anisotropic elastic tomography" in Treatise on Geophysics- Volume 1- Seismology and Structure of the Earth

Paris, 19 September 2008

Abstract

Major advances in Structural Seismology during the last twenty years, are related to the emergence and development of more and more sophisticated 3D imaging techniques, usually named seismic tomography, at different scales from local to global. Progress has been made possible by the rapid developments in seismic instrumentation and by the extensive use of massive computation facilities. The scope of this chapter is limited to the tomographic elastic structure of the upper mantle. In order to obtain a good spatial coverage of this part of the Earth, it is necessary to make use of dispersive properties of surface waves. Most global tomographic models are still suffering severe limitations in lateral resolution, due to the imperfect data coverage, and to crude theoretical approximations. It is usually assumed that the propagating elastic medium is isotropic, which is a poor approximation. It is shown in this chapter how to take account of anisotropy of Earth's materials and a complete tomographic technique including the resolution of the forward problem and of the inverse problem is presented. Consequently, by including other geological constraints, it is possible to map not only the 3D temperature heterogeneities but also the flow field within the convecting mantle. In order to improve the lateral resolution of global models, the installation of ocean bottom observatories is necessary and constitutes a new challenge for this new century. The next step will also consist in systematically applying recent developments in numerical modeling and theory to seismic data, in order to use the complete information provided by seismic waveforms and to incorporate physical and chemical constraints provided by other fields of earth sciences.

Keywords: Tomography, isotropic model, seismic anisotropy, S-wave splitting, surface waves, Rayleigh wave, Love wave, broadband seismology, normal modes, inverse problem, upper mantle, lithosphere, asthenosphere, transition zone.

Introduction

Twenty years ago, the first global isotropic tomographic models of the mantle were published (*Woodhouse and Dziewonski*, 1984; *Dziewonski*, 1984). Since that time, many new tomographic models were published, and a large family of techniques was made available. This important progress was made possible by the extensive use of computers which can handle very large datasets and by the availability of good quality digital seismograms recorded by broadband seismic networks such as GEOSCOPE (*Romanowicz et al.*, 1984), IRIS (*Smith*, 1986) and all networks coordinated by the FDSN (Federation of Digital Seismograph Networks; *Romanowicz and Dziewonski*, 1986). Thanks to the installation of modern digital networks, it is now possible to map the whole earth from the surface down to the center of the Earth by seismic tomography. However, most tomographic techniques only make use of travel times or phase information in seismograms and very few use the amplitude, even when seismic waveforms are used (*Woodhouse and Dziewonski*, 1984; *Li and Romanowicz*, 1996). Global tomographic models have been improved over years by an increase in the number of data and more importantly by using more general parameterizations, now including anisotropy (radial anisotropy in *Nataf et al.* (1986); general slight anisotropy in *Montagner and Tanimoto* (1990, 1991)) and to a lesser extent anelasticity (*Tanimoto*, 1989; *Romanowicz*, 1990). This chapter is focused on the imaging of large scale (>1000km) lateral heterogeneities of velocity and anisotropy in the upper mantle (0-660km depth) where the lateral resolution is the best thanks to surface waves providing an almost uniform lateral and azimuthal coverage, particularly below oceanic areas. We will discuss how tomographic imaging completely renewed our vision of upper mantle dynamics. It makes it possible to relate surface geology and plate tectonics to underlying mantle convection, and to map at depth the origin of geological objects such as continents, mountain ranges, slabs, ridges and plumes. The goal of this chapter is not to review all contributions to this topic, but to underline the main scientific issues, to present different approaches and to illustrate the different progress (partly subjectively) by some of my results or by other more recent models. This chapter aims to show why a major step, which takes a complete account of amplitude anomalies in the most general case and which will enable to map shorter scale heterogeneities, is now possible and presently ongoing.

1 Effects of seismic velocity and anisotropy on seismograms

For theoretical and practical reasons, the Earth was considered for a long time, as composed of isotropic and laterally homogeneous layers. While an isotropic elastic medium can be described by 2 independent

elastic parameters (λ and μ Lamé parameters), the cubic symmetry requires 3 parameters, but the most commonly used anisotropic medium (transverse isotropy with vertical symmetry axis) necessitates 5 independent parameters (*Love*, 1927: *Anderson*, 1961) and the most general elastic medium requires 21 independent parameters. However, since the sixties, it was recognized that most parts of the Earth are not only laterally heterogeneous but also anisotropic. Though the lateral heterogeneities of seismic velocities were used for a long time for geodynamical applications, the importance of anisotropy for understanding geodynamic processes has only been recognized recently.

Seismology is an observational field based on the exploitation of seismic recordings of the displacement (velocity or acceleration) of the Earth induced by earthquakes. Broadband 3-component high dynamic seismometers have been installed in more than 500 stations around the world during the last 20 years (see overview of Romanowicz and Dziewonski, this issue). Thanks to progress in instrumentation and theoretical developments, it is now possible to observe and to take a simultaneous account of the effects of lateral heterogeneities of velocity and anisotropy on seismograms.

1.1 First order perturbation theory

The basic equation which governs the displacement $\mathbf{u}(\mathbf{r}, t)$ is the elasto-dynamics equation:

$$\rho_0 \frac{d^2 u_i}{dt^2} = \sum_j \sigma_{ij,j} + F_{Ii} + F_{Ei} \tag{1}$$

F_{Ii} et F_{Ei} represent respectively the whole ensemble of applied inertial and external forces (see *Takeuchi and Saito* (1972) or *Woodhouse and Dahlen* (1978) for a complete description of all terms). Generally, by neglecting the advection term, this equation is written in a simple way:

$$(\rho_0 \partial_{tt} - H_0)\mathbf{u}(\mathbf{r}, t) = \mathbf{F}(\mathbf{r_S}, t) \tag{2}$$

where H_0 is an integro-differential operator and $\mathbf{F}$ expresses all forces applied to the source volume in $\mathbf{r_S}$ at time t (considered as external forces). $\mathbf{F}$ is assumed to be equal to 0 for $t < 0$. In the elastic case, there is a linear relationship between σ_{ij} and the strain tensor ϵ_{kl}. $\sigma_{ij} = \sum_{kl} \Gamma_{ijkl}\epsilon_{kl}$ (+ terms related to the initial stress). Γ_{ijkl} is a 4^{th}-order tensor, often written in its condensed form C_{ij} as a 6x 6 matrix. By using the different symmetry conditions $\Gamma_{ijkl} = \Gamma_{jikl} = \Gamma_{ijlk} = \Gamma_{klij}$, the tensor $\mathbf{\Gamma}$ is shown to have 21 independent elastic moduli in the most general anisotropic medium. In an isotropic medium, this number reduces to 2, the Lamé coefficients λ and μ.

When solving for the free oscillations of the Earth $\mathbf{F} = 0$. The solution $\mathbf{u}(\mathbf{r}, t)$ of equation (2) can be calculated for a spherically symmetric non rotating reference Earth model associated with the operator H_0, according to the equation:

$$\rho_0 \partial_{tt} \mathbf{u}(\mathbf{r}, t) = H_0 \mathbf{u}(\mathbf{r}, t) \tag{3}$$

The solution of equation (3) is beyond the scope of this chapter and is described elsewhere in the treatise (*Woodhouse*). The eigenvalues of the operator H_0 are equal to $-\rho_{0n}\omega_\ell^2$ where ${}_n\omega_\ell$ is the eigenfrequency characterized by 2 quantum numbers n and ℓ, respectively termed radial and angular orders. The corresponding eigenfunctions ${}_n\mathbf{u}_\ell^m(\mathbf{r}, t)$ depend on 3 quantum numbers n, ℓ, m, where m is the azimuthal order, with the following property $-\ell \leq m \leq \ell$. Therefore, for a given eigenfrequency ${}_n\omega_\ell$ calculated in a spherically symmetric Earth model, $2\ell + 1$ eigenfunctions can be defined. The eigenfrequency ${}_n\omega_\ell$ is said to be degenerate, with a degree of degeneracy $2\ell + 1$. There is a complete formal similarity with the calculation of the energy levels of the atom of hydrogen in quantum mechanics. The eigenfunctions ${}_n\mathbf{u}_\ell^m(\mathbf{r}, t)$ of the operator H_0 are orthogonal and normalized.

The important point is that the basis of functions ${}_n\mathbf{u}_\ell^m(\mathbf{r}, t)$ is complete. This implies that any displacement at the surface of the Earth can be expressed as a linear combination of these eigenfuctions:

$$\mathbf{u}(\mathbf{r}, t) = \sum_{n,\ell,m} {}_n a_\ell^m \, {}_n\mathbf{u}_\ell^m(\mathbf{r}, t)$$

Therefore, these eigenfunctions can be used to calculate the **synthetic** displacement at any point $\mathbf{r}$, at time t, due to a force system $\mathbf{F}$ in the source volume. For a point force $\mathbf{F}$ at point $\mathbf{r}_S$, a step time function and its associated moment tensor $\mathbf{M}$, which is a good starting model for earthquakes, the solution of the equation (2) is given by (*Gilbert*, 1971):

$$\mathbf{u}(\mathbf{r}, t) = \sum_{n,\ell,m} {}_n\mathbf{u}_\ell^m(\mathbf{r}) \, \frac{(1 - cos_n\omega_\ell t)}{{}_n\omega_\ell^2} e^{\frac{-{}_n\omega_\ell t}{2Q}} (\mathbf{M} : {}_n\epsilon_\ell^m)_{\mathbf{r_S}} \tag{4}$$

where ϵ is the deformation tensor. Since equation (4) is linear in $\mathbf{M}$, it can be easily generalized to more complex spatial and temporal source functions, and can be rewritten:

$$\mathbf{u}(\mathbf{r}, t) = \mathbf{G}(\mathbf{r}, \mathbf{r_S}, t, t_S)\mathbf{M}(\mathbf{r_S}, t_S)$$

where $\mathbf{G}(\mathbf{r}, \mathbf{r_S}, t, t_S)$ is the Green operator of the medium. Normal mode theory is routinely used to calculate synthetic seismograms at long periods ($T \geq 40s.$) and Centroid Moment Tensor solutions (*Dziewonski et al.*, 1981).

An example of real and synthetic seismograms is presented in **figure 1**. However, there are still some discrepancies (usually frequency dependent) between the observed and synthetic seismograms. The simplest way to explain the observed phase shifts (time delays) is to remove the assumption that the Earth is spherically symmetric, i.e. there are lateral heterogeneities between the source and the receiver. The next step is to characterize these lateral heterogeneities. Since the agreement between synthetic and observed seismograms is good at long periods ($T \geq 40s$), we can reasonably infer that the amplitude of heterogeneities is small ($< 10\%$). Behind the surface wave train, a long coda is usually observed, interpreted as scattered waves. However, when filtering out periods shorter than 40s, this coda vanishes, which means that the scattering effect is only large in the shallowest regions of the Earth (primarily the crust, and the upper lithosphere) but that it is probably negligible at larger depths. However, some groups are starting to use the information contained in these coda waves (*Aki and Richards*, 1980; *Snieder et al.*, 2002), and even from seismic noise (*Shapiro et al.*, 2005) for imaging the crust. For the sake of simplicity, our study is limited to long period surface waves and it is hypothesized that the scale of lateral heterogeneities is large compared with the seismic wavelength. This point will be discussed in section 2.1. A second hypothesis which must be discussed, is the isotropic nature of the Earth materials. Actually, it is a poor assumption, because seismic anisotropy can be unequivocally observed at different scales. Finally, the influence of lateral variations in attenuation must also be taken into account and will be discussed in another chapter (Seismic Attenuation in the Earth, *Romanowicz and Mitchell*, this volume).

1.2 Effect of anisotropic heterogeneities on normal modes and surface waves

Different geophysical fields are involved in the investigation of the manifestations of anisotropy of Earth materials: mineral physics and geology for the study of the microscopic scale, and seismology for scales larger than, typically, one kilometer. The different observations related to anisotropy, at different scales are reviewed in *Montagner* (1998) and in *Park and Maupin* (this volume).

Different kinds of observations have been used for investigating anisotropy in the upper mantle: the Rayleigh-Love wave discrepancy (*Anderson*, 1961), the azimuthal variation of phase velocities of surface waves (*Forsyth*, 1975) and the shear-wave splitting particularly for SKS waves (*Vinnik et al.*, 1992). The lack of stations in oceanic areas explains why it is necessary to use surface waves to investigate upper mantle structure (isotropic or anisotropic) at the global or regional scales.

In the simplest case (fundamental modes, no coupling between branches of Rayleigh and Love waves), the frequency shift $\frac{\delta\omega}{\omega}$ (and the corresponding phase velocity perturbation $\frac{\delta V}{V}$), for a constant wavenum-

ber k can be written by applying Rayleigh's principle:

$$\frac{\delta\omega}{\omega}|_k = \frac{\delta V}{V}|_k = \frac{1}{2\omega}\frac{\int_\Omega \epsilon^*_{ij}\,\delta\Gamma_{ijkl}\,\epsilon_{kl}\,d\Omega}{\int_\Omega \rho_{0n}\mathbf{u}^{m*}_\ell\,{}_n\mathbf{u}^m_\ell\,d\Omega} \tag{5}$$

where ϵ_{ij} and $\delta\Gamma_{ijkl}$ are respectively the deformation and the deviations of elastic tensor components from a SNREI model (spherically symmetric, non rotating, elastic, isotropic), and ${}_n\mathbf{u}^m_\ell$ the eigenfunctions as defined in the previous section.

We only consider the propagation of surface waves in a plane-layered medium for a general slight elastic anisotropy, but it can be easily extended to the spherical Earth (*Mochizuki*, 1986; *Tanimoto*,1986; *Romanowicz and Snieder*, 1988; *Larson et al.*, 1998; *Trampert and Woodhouse*, 2003). *Smith and Dahlen* (1973, 1975), found that, to first order in anisotropy and at frequency ω, the azimuthal variation of local phase velocity (Rayleigh or Love wave) can be expanded as a Fourier series of the azimuth Ψ along the path and is of the form:

$$\begin{aligned} V(\omega,\theta,\phi,\Psi) - V_0(\omega,\Psi) &= \alpha_0(\omega,\theta,\phi) + \alpha_1(\omega,\theta,\phi)cos2\Psi + \alpha_2(\omega,\theta,\phi)sin2\Psi \\ &\quad +\alpha_3(\omega,\theta,\phi)cos4\Psi + \alpha_4(\omega,\theta,\phi)sin4\Psi \end{aligned} \tag{6}$$

where $V_0(\omega,\Psi)$ is the reference velocity of the unperturbed medium, and Ψ is the azimuth along the path with respect to the North direction. *Montagner and Nataf* (1986) present the expressions for the different azimuthal coefficients $\alpha_i(\omega,\theta,\phi)$ as depth integral functions dependent on 13 simple linear combinations of standard cartesian elastic coefficients C_{ij}. The Appendix shows how to relate Γ_{ijkl} to C_{ij} and presents detailed calculation of azimuthal terms for Love waves in the geographical coordinate system.

Constant term (0 Ψ-azimuthal term: α_0)

$A = \rho V^2_{PH} = \frac{3}{8}(C_{11}+C_{22}) + \frac{1}{4}C_{12} + \frac{1}{2}C_{66}$

$C = \rho V^2_{PV} = C_{33}$

$F = \frac{1}{2}(C_{13}+C_{23})$

$L = \rho V^2_{SV} = \frac{1}{2}(C_{44}+C_{55})$

$N = \rho V^2_{SH} = \frac{1}{8}(C_{11}+C_{22}) - \frac{1}{4}C_{12} + \frac{1}{2}C_{66}$

2 Ψ-azimuthal term:

$\alpha_1 \cos 2\Psi$	$\alpha_2 \sin 2\Psi$
$B_c = \frac{1}{2}(C_{11}-C_{22})$	$B_s = C_{16}+C_{26}$
$G_c = \frac{1}{2}(C_{55}-C_{44})$	$G_s = C_{54}$
$H_c = \frac{1}{2}(C_{13}-C_{23})$	$H_s = C_{36}$

4 Ψ-azimuthal term:

$\alpha_3 \cos 4\Psi$	$\alpha_4 \sin 4\Psi$
$E_c = \frac{1}{8}(C_{11} + C_{22}) - \frac{1}{4}C_{12} - \frac{1}{2}C_{66}$	$E_s = \frac{1}{2}(C_{16} - C_{26})$

where indices 1 and 2 refer to horizontal coordinates (1: North; 2: East) and index 3 refers to vertical coordinate. ρ is the density, V_{PH}, V_{PV} are respectively horizontally and vertically *propagating* P-wave velocities, V_{SH}, V_{SV} horizontal and vertical *polarized* S-wave velocities. So, the different parameters present in the different azimuthal terms are simply related to elastic moduli C_{ij}.

From a practical point of view, once source phase is removed and assuming that the scale of heterogeneities is larger than the wavelength, the total phase ϕ_t (and the travel time) between the epicenter E and the receiver R, is easily related to the measurement of phase velocity $V_d(\omega)$, and therefore to the local phase velocity $V(\omega, \theta, \phi, \Psi)$:

$$\phi_t = \omega\, t_{E\to R} = \frac{\omega\Delta}{V_d(\omega)} = \omega \int_E^R \frac{ds}{V(\omega, \theta, \phi, \Psi)} \tag{7}$$

Therefore, equations (6) and (7) define the forward problem in the framework of first order perturbation theory. We will see in the next section how to solve the inverse problem. That means that, ideally, surface waves in the plane case have the ability to provide information on 13 elastic parameters, which emphasizes the enormous potential of surface waves in terms of geodynamical and petrological implications. There are only 13 elastic moduli among 21, since propagation of surface waves is invariant against rotation by π which corresponds to a monoclinic symmetry.

The 0-Ψ term corresponds to the average over all azimuths and involves 5 independent parameters, A, C, F, L, N, which represent the equivalent transversely isotropic medium with a vertical symmetry axis (more simply named VTI or radial anisotropy). It must be noted that it is possible to retrieve the equivalent isotropic shear modulus from these 5 parameters. By using a Voigt average, the shear modulus μ_{iso} is equal to:

$$\mu_{iso} = \rho V_{S_{iso}}^2 = \frac{1}{15}(C_{11} + C_{22} + C_{33} - C_{12} - C_{13} - C_{23} + 3C_{44} + 3C_{55} + 3C_{66})$$

According to the expressions of A, C, F, L, N in terms of elastic moduli, $\mu_{iso} = \frac{1}{15}(C+A-2F+6L+5N)$ So we can see that the equivalent isotropic velocity depends not only on V_{SV} and V_{SH}, but also on P-wave velocity and anisotropy ($\phi = \frac{C}{A}$) and on $\eta = \frac{F}{A-2L}$. By rewriting this expression $\mu_{iso} = \frac{1}{15}(C + (1-2\eta)A + (6+4\eta)L + 5N)$, neglecting anisotropy in P-wave ($\phi = 1$) and assuming $\eta = 1$, it is found that $\mu_{iso} = \rho V_{S_{iso}}^2 \approx \frac{2}{3}L + \frac{1}{3}N = \frac{2}{3}\rho V_{SV}^2 + \frac{1}{3}\rho V_{SH}^2$. Naturally, this choice is partly arbitrary, since usually, there is no S-wave anisotropy without P-wave anisotropy. Another way might consist

in using correlations between anisotropic parameters for petrological models as derived by *Montagner and Anderson* (1989a).

The other azimuthal terms (2-Ψ and 4-Ψ) depend on 4 groups of 2 parameters, B, G, H, E respectively describing the azimuthal variation of A, L, F, N. These simple parameters make it possible to describe in a simple way the two seismically observable effects of anisotropy on surface waves, the "polarization" anisotropy (*Schlue and Knopoff*, 1977) and the azimuthal anisotropy (*Forsyth*, 1975).

Another important point in these expressions is that they provide the partial derivatives for the radial and azimuthal anisotropy of surface waves. The corresponding kernels and their depth dependence are plotted in *Montagner & Nataf* (1986) (**Figures A2-A3**). These partial derivatives of the different azimuthal terms with respect to the elastic parameters can be easily calculated by using a radial anisotropic reference Earth model, such as *PREM* (*Dziewonski and Anderson*, 1981). The partial derivatives of the eigenperiod ${}_0T_\ell$ with respect to parameter p, $\frac{p}{T}\frac{\partial T}{\partial p}$ can easily be converted into phase velocity partial derivatives by using:

$$\frac{p}{V}(\frac{\partial V}{\partial p})_T = -\frac{V}{U}\frac{p}{T}(\frac{\partial T}{\partial p})_k$$

For example, the parameters G_c and G_c have the same kernel as parameter L (related to V_{SV}) as shown by comparing the expressions ofR_1, R_2 and R_3 in equation (29) of Appendix. For fundamental modes, the calculation of kernels shows that Love waves are almost insensitive to V_{SV} (Figure A2) and Rayleigh waves to V_{SH}. Rayleigh waves are the most sensitive to SV-waves. However, as pointed out by *Anderson and Dziewonski* (1982), the influence of P-waves (through parameters A and C) can be very large in an anisotropic medium. The influence of density is also very large for Love and Rayleigh waves, but as shown by *Takeuchi and Saito* (1972), it is largely decreased when seismic velocities are inverted for, instead of elastic moduli and density.

1.3 Comparison between surface wave anisotropy and SKS splitting data

It can be noted that some of the linear combinations of elastic moduli C_{ij}, derived from surface waves in the previous section, also come up when considering the propagation of body waves in symmetry planes for a weakly anisotropic medium (see for example *Crampin et al.* (1984) and their azimuthal dependence

$\rho V_P^2 = A + B_c \cos 2\Psi + B_s \sin 2\Psi + E_c \cos 4\Psi + E_s \sin 4\Psi$

$\rho V_{qSH}^2 = N - E_c \cos 4\Psi - E_s \sin 4\Psi$

$\rho V_{qSV}^2 = L + G_c \cos 2\Psi + G_s \sin 2\Psi$

where V_{qSH} and V_{qSV} corresponds respectively to quasi-SH and quasi-SV waves.

A global investigation of anisotropy inferred from SKS body wave splitting measurements (delay times and directions of maximum velocities) has been undertaken by different authors (*Vinnik et al.*, 1992; *Silver*, 1996; *Savage*, 1999). Unfortunately, most SKS measurements have been done in continental parts of the Earth, and very few in oceans. It turns out that a direct comparison of body wave and surface wave datasets is now possible (*Montagner et al.*, 2000). If the anisotropic medium is assumed to be characterized by a horizontal symmetry axis with any orientation (that is a very strong assumption which can be alleviated as shown by *Chevrot et al.*, 2004), and for a vertically propagating SKS wave, a synthetic dataset of SKS delay times and azimuths can be calculated from the global distribution of anisotropy derived from surface waves, by using the following equations:

$$\delta t_{SKS} = \int_0^h dz \sqrt{\frac{\rho}{L}} [\frac{G_c(z)}{L(z)} cos(2\Psi(z)) + \frac{G_s(z)}{L(z)} sin(2\Psi(z))] \tag{8}$$

where δt_{SKS} is the integrated travel time for the depth range *0-h* for a propagation azimuth Ψ, where the anisotropic parameters $G_c(z)$,$G_s(z)$ and $L(z)$ are the anisotropic parameters retrieved from surface waves at different depths. It is remarkable to realize that only the *G*-parameter (expressing the SV-wave azimuthal variation) is present in this equation. From equation (8), we can infer the maximum value of delay time δt_{SKS}^{max} and the corresponding azimuth Ψ_{SKS}:

$$\delta t_{SKS}^{max} = \sqrt{\left\{ \int_0^h dz \sqrt{\frac{\rho}{L}} \frac{G_c(z)}{L(z)} \right\}^2 + \left\{ \int_0^h dz \sqrt{\frac{\rho}{L}} \frac{G_s(z)}{L(z)} \right\}^2} \tag{9}$$

$$tan(2\Psi_{SKS}) = \frac{\int_0^h dz \frac{G_s(z)}{L(z)}}{\int_0^h dz \frac{G_c(z)}{L(z)}} \tag{10}$$

However, equation (8) is approximate and only valid when the wavelength is much larger than the thickness of layers. It is possible to make more precise calculations by using the technique derived for 2 layers by *Silver & Savage* (1994) or by using the general expressions given in *Rumpker and Silver* (1998), *Montagner et al.* (2000), *Chevrot et al.*, 2004).

With equations (9) and (10), a synthetic map of the maximum value of delay time δt_{SKS}^{max} can be obtained by using an 3D anisotropic surface wave model. A detailed comparison between synthetic SKS derived from AUM (*Montagner & Tanimoto*, 1991) and observed SKS (*Silver*, 1996) was presented in *Montagner et al.* (2000). **Figure 2** shows such a map for the Earth centered in the Pacific, by using the anisotropic surface wave model of *Montagner* (2002) derived from the data of *Montagner and Tanimoto* (1991) and *Ekström et al.* (1997). First of all, the comparison shows that both datasets are

compatible in magnitude but not necessarily in directions. Some contradictions between measurements derived from surface waves and from body waves have been noted. The agreement of directions is correct in tectonically active areas but not in old cratonic zones. The discrepancy in these areas results from the rapid lateral change of directions of anisotropy at a small scale. These changes stem from the complex history of these areas, which have been built by successive collages of continental pieces. It might also result from the hypothesis of horizontal symmetry axis, which was shown to be invalid in many areas (*Plomerova et al.*, 1996). The positive consequence of this discrepancy is that a small scale mapping of fossile anisotropy in such areas might provide clues for understanding the processes of growth of continents and mountain building opening a new field, the paleoseismology.

Unloke surface waves, SKS-waves have a good lateral resolution, and are sensitive to the short wavelength anisotropy just below the stations. But their drawback is that they have a poor vertical resolution. On the other hand, global anisotropy tomography derived from surface waves only provides long wavelength anisotropy (poor lateral resolution) but enables the location at depth of anisotropy. The long wavelength anisotropy derived from surface waves will display the same direction as the short wavelength anisotropy inferred from body waves only when large scale vertical coherent processes are predominant. As demonstrated by *Montagner et al.* (2000), the best agreement between observed and synthetic SKS can be found when only layers in the uppermost 200km of the mantle are taken into account. Moreover, tomographic models derived from surface waves looses resolution at depths greater than 200km. In some continental areas, short scale anisotropy, the result of a complex history, might be important and even might mask the large-scale anisotropy more related to present convective processes (see for example *Marone and Romanowicz*, 2006 for North America). From a statistical point of view, good agreement is found between orientations of anisotropy and plate velocity motion for fast-moving plates. The differences between anisotropy and tectonic plate directions are related to more complex processes, as will be seen in section 3.

2 Upper mantle tomography of seismic velocity and anisotropy

We now show how to implement theory of section 1 from a practical but general point of view, and how to design a tomographic technique in order to invert for the 13 different elastic parameters and density. A tomographic technique necessitates to solve simultaneously a forward problem and an inverse problem. By using the results of the previous section, it successively considers how to set the forward problem, and how it is used to retrieve a set of parameters by inversion.

2.1 Forward problem

First, it is necessary to define the data space **d** and the parameter space **p**. It is assumed that a functional **g** relating **d** and **p** can be found such that:

$\mathbf{d} = \mathbf{g}(\mathbf{p})$,

where **d** is the set of data (which samples the data space), and **p** the set of parameters.

Data Space: **d**

The basic dataset is made of seismograms $\mathbf{u}(t)$. We can try to directly match the waveform in the time domain, or we can work in the Fourier domain, by separating phase and amplitude on each component $u_i(t)$:

$$u_i(t) = \int_{-\infty}^{\infty} A_i(\omega) e^{i(\omega t - \phi_i)} d\omega$$

The approach consisting in fitting seismic waveforms is quite general but, from a practical point of view, it does not necessarily correspond to the simplest choice. In a heterogeneous medium, the calculation of amplitude and phase effects makes it necessary to calculate the coupling between different multiplets (*Li and Tanimoto*, 1993; *Li and Romanowicz*, 1995; *Marquering et al.*, 1996), which is very time consuming. When working in Fourier domain, different time windows can be considered and the phase of different seismic trains, body waves and surface waves can be separately matched (*Nolet*, 1990; *Lévêque et al.*, 1991) under drastic simplifying assumptions. **Figure 1** showed an example of observed and synthetic seismograms, the latter obtained by normal mode summation with the different higher modes. The fundamental wavetrain is well separated from other modes at large epicentral distances. The part of the seismogram corresponding to higher modes is more complex and shows overlap of these modes in the time domain. Therefore, from a practical point of view, the fitting of the fundamental mode wavetrain will not cause any problem and has been widely used in global mantle tomography. The use of higher mode wavetrains and the separation of overtones is much more difficult. The first attempts were performed by *Nolet* (1975), *Cara* (1978), *Okal and Jo* (1985) and *Dost* (1990) by applying a spatial filtering method. Unfortunately, all these techniques can only be applied in areas where dense arrays of seismic stations are present, i.e. in North America and Europe. By using a set of seismograms recorded at one station but corresponding to several earthquakes located in a small source area, *Stutzmann and Montagner* (1993) showed how to separate the different higher modes. A similar approach was also followed by *Van Heijst and Woodhouse* (1997). We only detail in this paper the technique which was designed for fitting the fundamental mode wavetrain and the reader is referred to *Stutzmann and Montagner* (1993, 1994), *Van Heijst and Woodhouse* (1997) and *Beucler et al.* (2003) for the description of the recovery of higher mode dispersion properties and to *Romanowicz*

(2002) for a general overview. **Figure 3** presents an example of phase velocity dispersion for different surface wave modes (fundamental and first higher modes (*Beucler et al.*, 2003)) and how they compare with previous investigations (*Cara*, 1978; *Van Heijst and Woodhouse*, 1997).

We take advantage of the fact that, according to the Fermat's principle, the phase velocity perturbation is only dependent to second order on path perturbations, whereas amplitude perturbation are dependent, to first order, on these perturbations, which implies that the eigenfunctions must be recalculated at each iteration. Therefore, the phase is a more robust observable than the amplitude. The amplitude $A(\omega)$ depends in a complex manner on seismic moment tensor, attenuation, scattering, focusing effects, station calibration and near-receiver structure whereas the contribution of lateral heterogeneities of seismic velocity and anisotropic parameters to the phase $\phi(\omega)$ can be easily extracted. The dataset under investigation, is composed of propagation times (or phase velocity measurements for surface waves) along paths: $\mathbf{d} = \{\frac{\Delta}{V(\omega)}\}$.

On the other hand, the phase of a seismogram at time t is decomposed, as follows: $\phi = \mathbf{k}.\mathbf{r} + \phi_0'$, where $\mathbf{k}$ is the wave vector, ϕ_0' is the initial phase including several terms: $\phi_0' = \phi_0 + \phi_S + \phi_I$, ϕ_S is the initial source phase, ϕ_0 is related to the number of polar phase shifts, ϕ_I is the instrumental phase. ϕ can be measured on seismograms by Fourier transform. We usually assume that ϕ_S is correctly given by the centroid moment tensor solution. For a path between epicenter E and receiver R with an epicentral distance Δ, the phase ϕ is given by:

$$\phi = \frac{\omega\Delta}{V_{obs}} + \phi_0 + \phi_S + \phi_I \tag{11}$$

In the general case, we want to relate the observed phase velocity $V_{obs}(\omega)$ to the parameters of the Earth model $\mathbf{p}(\mathbf{r}, \theta, \phi)$. Data and 3D parameters can be related through integrals over the whole volume of the Earth. But for computing reasons, it is usual to use a multistep approach, where we first retrieve the local phase velocity $V(\omega, \theta, \phi)$ including its azimuthal terms, and then perform the inversion at depth. These 2 steps can be reversed since the order of the integrations can be reversed. It is necessary to consider the nature of the perturbed medium. Following the approach of *Snieder* (1988), if the perturbed medium is at the same time smooth (long wavelength heterogeneities) and weak (small amplitude of heterogeneities), the geometrical optics approximation (and ray theory) applies. This hypothesis is not necessarily met within the Earth where some geological objects (slabs, mantle plumes, ...) have a length scale which can be close to the seismic wavelength. In the approximation of ray theory, the volume integral reduces to the curvilinear integral along the geometrical ray path.

When ray theory is applicable:

$$\phi - \phi_0' = \frac{\omega\Delta}{V_{obs}(\omega)} = \int_E^R \frac{\omega ds}{V(\omega,\theta,\phi)} \tag{12}$$

Where the integral is evaluated along the ray path between the epicenter E and the receiver R. Following the results of the previous section, different approximations are implicitly made when using this expression of the phase:

• large angular order $\ell \gg 1$, but not too large (scattering problems). From a practical point of view, this means that measurements are performed in the period range 40s $< T <$ 200s with seismic wavelengths between 200 and 1000km.

• geometrical optics approximation: If λ is the wavelength of the surface wave at period T, and Λ_S the spatial wavelength of heterogeneity: $\Lambda_S \gg \lambda = VT \Rightarrow \Lambda_S \gtrsim 2000km$. Epicentral distance Δ must be larger than seismic wavelength.

• slight anisotropy and heterogeneity: $\frac{\delta V}{V} \ll 1$. According to *Smith and Dahlen* (1973) for the plane case, the local phase velocity can be decomposed as a Fourier series of the azimuth Ψ (equation 6): Each azimuthal term $\alpha_i(T,\theta,\phi)$ of equation (6) can be related to the set of parameters $p_i(r,\theta,\phi)$ (density + 13 elastic parameters), according to the expressions derived in Appendix.

$$\begin{aligned}\frac{\Delta}{V_{obs}(T)} - \frac{\Delta}{V_0(T)} \quad = -\sum_{j=0}^{2}\sum_{i=1}^{14} \quad & \int_E^R \frac{ds}{V_0}\int_0^a \left[\left(\frac{p_i}{V}\frac{\partial V}{\partial p_i}\right)_j \frac{\delta p_i(r,\theta,\phi)}{p_i}\cos(2j\Psi)\right. \\ & \left. + \left(\frac{p_i}{V}\frac{\partial V}{\partial p_i}\right)_j \frac{\delta p_i(r,\theta,\phi)}{p_i}\sin(2j\Psi)\right]\frac{dz}{\Delta h}\end{aligned} \tag{13}$$

Equation (13) defines the forward problem in the framework of first order perturbation theory, relating the data and the parameter spaces. This approach is usually named PAVA (Path average approximation). Many terms in equation (13) are equal to zero since all parameters are not present in each azimuthal term. A last important ingredient in the inverse problem formulation is the "structure" of the data space. It is expressed through its covariance function (continuous case) or covariance matrix (discrete case) of data C_d. When data d_i are independent, C_d is diagonal and its elements are the square of the errors on data σ_{d_i}.

-Finite-frequency effects

As mentioned previously, a strong hypothesis is that in the framework of geometrical optics approximation, only large scale heterogeneities can be retrieved. But interesting geological objects such as slabs, plumes are smaller scale. To go beyond the ray theory, it is necessary to take account of the

finite-frequency effect when scale length has the same order of magnitude as the seismic wavelength. It is possible to use the scattering theory based on the Born or Rytov approximations (see for example *Woodhouse and Girnius* (1982) for normal mode approach, *Snieder* (1988) for surfaces waves, *Yomogida* (1992), *Dahlen et al.* (2000) for body waves). Equation (13) shows that the sensitivity kernels are 1D, meaning that only heterogeneities in the vertical plane containing the source and the receiver are taken into account, whereas, by using the scattering theory, it is possible to calculate 3D kernels and consequently to take account of off-path heterogeneities. The equations (12) and (13) must be replaced by an integral over the volume Ω:

$$\frac{\Delta}{V_{obs}(T)} - \frac{\Delta}{V_0(T)} = \sum_{i=1}^{14} \int\int\int_{\Omega} K_i(T,\theta,\phi) \frac{\delta p_i(r,\theta,\phi)}{p_i} d\Omega \tag{14}$$

where $K(T,\theta,\phi)$ is the scattering Fréchet sensitivity kernel, which depends on wave type (Rayleigh or Love) and on the relative location of E and R (see for example *Romanowicz*, 2002 for a review). Very different strategies can be followed for calculating this triple integral, by separating the surface integral and the radial integral. Marqueing

Parameter space: $\mathbf{p}(\mathbf{r})$

It is quite important to thoroughly think of the structure of the parameter space. First of all, it is necessary to define which parameters are required to explain our dataset, how many **physical parameters** can be effectively inverted for, in the framework of the theory that is considered. For example, if the Earth is assumed to be elastic, laterally heterogeneous but isotropic, only 3 independent physical parameters, V_P, V_S and density ρ (or the elastic moduli λ, μ and ρ) can be inverted for, from surface waves. In a transversely isotropic medium with a vertical symmetry axis (*Anderson*, 1961; *Takeuchi and Saito*, 1972), the number of independent physical parameters is now 6 (5 elastic parameters + density). In the most general case of a weak anisotropy, 14 physical parameters (13 combinations of elastic moduli + density) can actually be inverted for, using surface waves. Therefore, the number of "physical" parameters p_i depends on the underlying theory which is used for explaining the dataset.

Once the number of "physical" independent parameters is defined, we must define how many "**spatial**" (or geographical) parameters are required to describe the 3D distributions $p_i(r,\theta,\phi)$. That is a difficult problem because the number of "spatial" parameters which can be reliably retrieved from the dataset, is not necessarily sufficient to provide a correct description of $p_i(r,\theta,\phi)$, i.e. of the real Earth. The correct description of $p_i(r,\theta,\phi)$ depends on its spectral content: for example, if $p_i(r,\theta,\phi)$

is characterized by very large wavelengths, only a small number of spatial parameters is necessary, but if $p_i(r, \theta, \phi)$ presents very small-scale features, the number of spatial parameters will be very large. In any case, it is necessary to assess the range of possible variations for $p_i(r, \theta, \phi)$ in order to provide some bounds on the parameter space. This is done through a covariance function of parameters in the continuous case (or a covariance matrix for the discrete case) $C_{p_i p_j}(\mathbf{r}, \mathbf{r}')$ at 2 different points $\mathbf{r}$, $\mathbf{r}'$. These *a priori* constraints can be provided by other fields in geosciences, geology, mineralogy, numerical modeling...

Consequently, a tomographic technique must not be restricted to the inversion of parameters $\mathbf{p} = \{p_i(r, \theta, \phi)\}$ that are searched for, but must include the calculation of the final covariance function (or matrix) of parameters C_p. That means that the retrieval of parameters is contingent to the resolution and the errors of the final parameters and is largely dependent on the resolving power of data (*Backus and Gilbert*, 1967, 1968, 1970). Finally, the functional $\mathbf{g}$ which expresses the theory relating the data space to the parameter space is also subject to uncertainty. In order to be completely consistent, it is necessary to define the domain of validity of the theory and to assess the error σ_T associated with the theory. *Tarantola and Valette* (1982) showed that the error σ_T is simply added to the error on data σ_d.

2.2 Inverse problem

So far, we did not make assumption on the functional $\mathbf{g}$ relating data and parameters. But in the framework of first order perturbation theory, the forward problem is usually linearized and the equation (13) can be simply written in the linear case:

$$\mathbf{d} = \mathbf{G}\mathbf{p}$$

where $\mathbf{G}$ is now a matrix (or a linear operator) composed of Fréchet derivatives of $\mathbf{d}$ with respect to $\mathbf{p}$, which has the dimensions $n_d \times n_p$ (number of data $\times$ number of parameters). This matrix usually is not square and many different techniques in the past have been used for inverting $\mathbf{G}$. In any case, the inverse problem will consist in finding an inverse for the functional $\mathbf{g}$, that we will write $\tilde{\mathbf{g}}^{-1}$, notwithstanding the way it is obtained, such that:

$$\mathbf{p} = \tilde{\mathbf{g}}^{-1}(\mathbf{d})$$

To solve the inverse problem, different algorithms can be used.The least-squares solution is usually solved by minimizing a cost function J. Making symmetric the data space and the parameter space,

Tarantola and Valette (1982) are defining the cost function J as:

$$J = (\mathbf{d} - \mathbf{Gp})^t C_d^{-1} (\mathbf{d} - \mathbf{Gp}) + (\mathbf{p} - \mathbf{p_0})^t C_p^{-1} (\mathbf{p} - \mathbf{p_0})$$

The first term corresponds to classical least-squares with no damping, whereas the second term corresponds to norm damping, which imposes smoothness upon the parameter space. Different choices were proposed for this second term. For example *Montagner* (1986b) is using a Gaussian covariance function characterized by a correlation length and an *a priori* error σ_p on parameters whereas *Su et al.* (1984) prefer to minimize the roughness of the model. Other choices consist in taking a constant value such that $\delta\mathbf{p}^t C_p^{-1} \delta\mathbf{p} = \lambda^2 \delta\mathbf{p}^t \delta\mathbf{p}$ (*Yoshizawa and Kennett*, 2004). Or the covariance operator can be replaced by a Laplacian operator (see for example *Zhou et al.*, 2006):

$$\delta\mathbf{p}^t C_p^{-1} \delta\mathbf{p} = \epsilon \left(\int\int\int |\nabla^2 (\frac{\delta p}{p})|^2 d\Omega \right)^{1/2}$$

A discussion about damping can be found in *Trampert and Snieder* (1996) who prefer Laplacian over model damping to reduce the spectral leakage.

As an example, by using the expression of J, a quite general and widely used algorithm has been derived by *Tarantola and Valette* (1982):

$$\begin{aligned} \mathbf{p} - \mathbf{p_0} &= (G^t C_d^{-1} G + C_{p_0}^{-1})^{-1} G^t C_d^{-1} (\mathbf{d} - \mathbf{g}(\mathbf{p}) + G(\mathbf{p} - \mathbf{p_0})) \\ &= C_{p_0} G^t (C_d + G C_{p_0} G^t)^{-1} (\mathbf{d} - \mathbf{g}(\mathbf{p}) + G(\mathbf{p} - \mathbf{p_0})) \end{aligned} \quad (15)$$

where C_d is the covariance matrix of data, C_{p_0} the covariance function of parameters $\mathbf{p}$, and G is the Frechet derivative of the operator $\mathbf{g}$ at point $\mathbf{p}(\mathbf{r})$. This algorithm can be made more explicit by writing it in its integral form:

$$\mathbf{p}(\mathbf{r}) = \mathbf{p_0}(\mathbf{r}) + \sum_i \sum_j \int_V d\mathbf{r}' C_{p_0}(\mathbf{r}, \mathbf{r}') G_i(\mathbf{r}') (S^{-1})_{ij} F_j \quad (16)$$

with $S_{ij} = C_{d_{ij}} + \int_V d\mathbf{r_1} d\mathbf{r_2}\, G_i(\mathbf{r_1}) C_{p_0}(\mathbf{r_1}, \mathbf{r_2}) G_j(\mathbf{r_2})$, $F_j = d_j - g_j(\mathbf{p}) + \int_V d\mathbf{r}"\, G_j(\mathbf{r}")(\mathbf{p}(\mathbf{r}") - \mathbf{p_0}(\mathbf{r}"))$
This algorithm can be iterated and is suited for solving slightly non-linear problems. Different strategies can be followed to invert for the 3D-models $\mathbf{p}(\mathbf{r})$, because the size of the inverse problem is usually enormous in practical applications and a compromise must be found between resolution and accuracy (and also computing time). For the example of mantle tomography, a *minimum* parameter space will be composed of 13 (+density) physical parameters multiplied by 30 layers (if the mantle is divided into 30 independent layers. If geographical distributions of parameters are searched for up to

degree 40 (lateral resolution around 1000km), that implies a number of about $700,000$ independent parameters. Such a problem is still very hard to handle from a computational point of view. A simple approach for solving this problem consists in dividing the inversion procedure into 2 steps. The first step consists in regionalizing phase (or group) velocity data in order to retrieve the different azimuthal terms, and the second step is the inversion at depth. It was implemented by *Montagner* (1986a,b) and a very similar technique is presented by *Barmin et al.* (2001). In case of a large dataset, *Montagner and Tanimoto* (1990) showed how to handle the inverse problem by making a series expansion of the inverse of matrix S. It was recently optimized from a computational point of view by *Debayle and Sambridge* (2004) and *Beucler and Montagner* (2005). One advantage of this technique is that it can be applied indifferently to regional studies or global studies. In case of imperfect spatial coverage of the area under investigation, it does not display ringing phenomena commonly observed when a spherical harmonics expansion is used (*Tanimoto*, 1986).

From a practical point of view, the choice of the model parameterization is also very important and different possibilities can be considered:

• Discrete basis of functions:

A simple choice consists in dividing the earth into 3D blocks with a surface block size different from the radial one. The size of block depends on the lateral resolution expected from the path coverage. A variant of this parameterization is the use of a set of spherical triangular grid points (see for example *Zhou et al.*, 2006). The block decomposition is valid as well for global investigations as for regional studies. Usually, the Earth surface parameterization is different for the radial one. For global study, the natural basis is composed of the spherical harmonics for the horizontal variations $p_i(r,\theta,\phi) = \sum_{\ell=0}^{\ell_{max}} \sum_{m=-\ell}^{\ell} a_l^m(r) Y_\ell^m(\theta,\phi)$. Other choices are possible, such as spherical splines (*Wang and Dahlen*, 1995). When data coverage is very uneven, other strategies are proposed using irregular cells or adaptative meshes (see for example *Zhang and Thurber* (2005)).

• Continuous function $\mathbf{p}(\mathbf{r})$. In that case, the function is directly inverted for. Since the number of parameters is then infinite, it is necessary to regularize the solution by defining a covariance function of parameters $C_{p_0}(\mathbf{r},\mathbf{r'})$. For the horizontal variations, a Von Mises distribution (*Fisher*, 1953; *Montagner*, 1986b) can be used for initial parameters $\mathbf{p_0}(\mathbf{r})$:

$$C_{p_0}(\mathbf{r},\mathbf{r'}) = \sigma_p(\mathbf{r})\sigma_p(\mathbf{r'}) \exp \frac{\cos \Delta_{\mathbf{rr'}} - 1}{L_{cor}^2} \approx \sigma_p(\mathbf{r})\sigma_p(\mathbf{r'}) \exp \frac{-\Delta_{\mathbf{rr'}}^2}{2L_{cor}^2}$$

where L_{cor} is the correlation length which will define the smoothness of the final model. This kind of distribution is well suited for studies on a sphere and is asymptotically equivalent to a Gaussian distribution when $L_{cor} \ll a$ (a radius of the Earth). When different azimuthal terms distributions are

searched for, it is possible to define cross-correlated covariance functions of parameters $C_{p_i p_j}(\mathbf{r}, \mathbf{r}')$, but since the different terms of the Fourier expansion in azimuth correspond to orthogonal functions, the cross-correlated terms off the diagonal can be taken equal to zero.

It is interesting to note that, in equation (16), the Frechet derivatives G along the path are multiplied by the Gaussian covariance operator C_{p_0} . It means that the technique, which can be named "Gaussian" tomography, is equivalent to use "fat" rays: when the correlation length is wider than the Fresnel zone, ray theory applies, and consequently, the finite-frequency effects can be neglected. As discussed by *Ritzwoller et al.* (2002) and *Sieminski et al.* (2004), there might be some slight differences in amplitude between Gaussian tomography and Diffraction tomography (taking account of finite-frequency effects), but not in the location of heterogeneities provided that the spatial path coverage is sufficiently dense. The radial parameterization must be related to the resolving capability of the data at depth, according to the frequency range under consideration. For the radial variations, polynomial expansions can be used (see for example *Dziewonski and Woodhouse*, (1987) for Tchebyshev polynomials, or *Boschi and Ekström* (2002) for radial cubic splines). Since the number of physical parameters is very large for the inversion at depth, physical parameters are usually correlated. The different terms of the covariance function C_p between parameters p_1 and p_2 at radii r_i and r_j can be defined as follows:

$$C_{p_1,p_2}(r_i, r_j) = \sigma_{p_1}(r_i)\sigma_{p_2}(r_j)\zeta_{p_1,p_2} \exp -\frac{(r_i - r_j)^2}{2L_{r_i}L_{r_j}}$$

Where ζ_{p_1,p_2} is the correlation between physical parameters p_1 and p_2 inferred for instance from different petrological models (*Montagner and Anderson*, 1989a) such as pyrolite (*Ringwood*, 1975) and piclogite (*Anderson and Bass*, 1984; and *Bass and Anderson*, 1984). L_{r_i}, L_{r_j} are the radial correlation lengths which are used to smooth the inverse model.

The *a posteriori* covariance function is given by:

$$C_p = C_{p_0} - C_{p_0}G^T(C_d + GC_{p_0}G^T)^{-1}GC_{p_0} = (G^T C_d^{-1} G + C_{p_0}^{-1})^{-1} \tag{17}$$

The resolution R of parameters can be calculated as well. It corresponds to the impulsive response of the system: $\mathbf{p} = \tilde{\mathbf{g}}^{-1}\mathbf{d} = \tilde{\mathbf{g}}^{-1}\mathbf{g}\,\mathbf{p}' = R\,\mathbf{p}'$. If the inverse problem is perfectly solved, R is the identity function or matrix. However, the following expression of resolution is only valid in the linear case (*Montagner and Jobert*, 1981):

$$R = C_{p_0}G^T(C_d + GC_{p_0}G^T)^{-1}G = (G^T C_d G + C_{p_0})^{-1}G^T C_d^{-1} G \tag{18}$$

It is interesting to note, that the local resolution of parameters is imposed by both the correlation length and the path coverage, unlike the *Backus-Gilbert* (1967, 1968) approach, which primarily de-

pends on the path coverage. The effect of a damping factor in the algorithm to smooth the solution, is equivalent to the introduction of a simple covariance function on parameters weighted by the errors on data (*Ho-Liu et al.*, 1989). When the correlation length is chosen very small, the algorithms of *Backus-Gilbert* (1968, 1970) and *Tarantola and Valette* (1982) are equivalent.

By considering the *a posteriori* covariance function and the resolution, it is possible to assess the reliability of the hypotheses made about the independence of parameters. For example *Tanimoto and Anderson* (1985) and *Montagner and Jobert* (1988) showed that there is a trade-off between azimuthal terms and constant term in case of a poor azimuthal coverage. For the inversion at depth *Nataf et al.* (1986) also display the trade-off between physical parameters V_{PH}, V_{SV}, ξ, ϕ and η when only Rayleigh and Love wave $0 - \Psi$-terms are used in the inversion process.

Though 13 elastic parameters (+ density) are necessary to explain surface wave data (Rayleigh and Love waves), only 4 parameters are well resolved for small anisotropy (*Montagner and Jobert*, 1988): the azimuthally averaged S-wave velocity V_S, the radial anisotropy expressed through the ξ parameter ($\xi = (V_{SH}/V_{SV})^2$) where V_{SH} (resp. V_{SV}) is the velocity of S-wave propagating horizontally with horizontal transverse polarization (resp. with vertical polarization), and the $\mathbf{G}$ (G_c, G_s) parameters expressing the horizontal azimuthal variation of V_{SV}. ξ was introduced in the reference Earth model PREM (*Dziewonski and Anderson*, 1981) down to 220km in order to explain a large dataset of free oscillation eigenfrequencies and body wave travel times. The other elastic parameters can be derived, by using constraints from petrology in order to reduce the parameter space (*Montagner & Anderson*, 1989a). This approach was followed by *Montagner & Anderson* (1989b) to derive an average reference earth model, and by *Montagner & Tanimoto* (1991) for the first global 3-D anisotropic model of the upper mantle.

2.3 Isotropic and anisotropic images of the upper mantle

The complete anisotropic tomographic procedure has been implemented for making different regional and global studies. Many global isotropic tomographic models of the upper mantle were published since *Wooodhouse and Dziewonski* (1984) and the recent results have been reviewed by *Romanowicz* (2003). Many models inverting only for radial anisotropy but neglecting azimuthal anisotropy, have also been published (*Nataf et al.*, 1984, 1986; *Ekström and Dziewonski*, 1998; *Shapiro and Ritzwoller*, 2002, *Gung et al.*, 2003; *Panning and Romanowicz*, 2004; *Zhou et al.*, 2006) The complete anisotropic tomographic technique (including azimuthal anisotropy) has been applied for investigating the upper mantle structure either at a regional scale of the Indian Ocean (*Montagner*, 1986a; *Montagner and*

Jobert, 1988; *Debayle and Lévêque*, 1997), of the Atlantic Ocean (*Mocquet and Romanowicz*, 1989; *Silveira et al.*, 1998; *Silveira and Stutzmann*, 2002), of Africa (*Hadiouche et al.*, 1989; *Debayle et al.*, 2001; *Sebai et al.*, 2005; *Sicilia et al.*, 2005), of Pacific Ocean (*Nishimura & Forsyth*, 1989; *Bussy et al.*, 1993; *Montagner*, 2002; *Ritzwoller et al.*, 2004), of Antarctica (*Roult et al.*, 1994), Australia (*Debayle and Kennett*, 2000; *Simons et al.*, 2002) and Central Asia (*Griot et al.*, 1998a,b; *Villaseñor et al.*, 2001) or at a global scale (*Montagner & Tanimoto*, 1990, 1991; *Montagner*, 2002; *Debayle et al.*, 2004). The reader is also referred to a quantitative comparison of tomographic and geodynamic models by *Becker and Boschi* (2002).

An important issue, when constructing tomographic models is the correction for crustal structure, where sedimentary thickness, Moho depth variations are so strong that they affect dispersion of surface waves at least up to 100s : it was shown (*Montagner and Jobert*, 1988) that standard perturbation theory is inadequate to correct for crustal correction and more rigorous approaches were proposed (*Li and Romanowicz*, 1996); *Boschi and Ekström*, 2002; *Zhou et al.*, 2005) using the updated crustal models 3SMAC (*Nataf and Ricard*, 1996; *Ricard et al.*, 1996) or CRUST2.0 (*Mooney et al.*, 1998; *Laske et al.*, 2001).

As an example of the results obtained after the first step of the tomographic procedure, **Figure 4** shows different maps of $2-\Psi$ azimuthal anisotropy for Rayleigh waves at 100s period for the first 3 modes, n=0,1,2 superimposed on the isotropic part ($0-\Psi$ term) of phase velocity (*Beucler and Montagner*, 2006). From petrological and mineralogical considerations, *Montagner and Nataf* (1988) and *Montagner and Anderson* (1989a,b) showed that the predominant terms of phase velocity azimuthal expansion are the 0-Ψ and 2-Ψ for Rayleigh waves, and 0-Ψ and 4-Ψ for Love waves. However, *Trampert and Woodhouse* (2003) carefully addressed the requirement of azimuthal anisotropy, and demonstrated that Rayleigh wave data need both 2Ψ and 4Ψ terms, which is also confirmed by *Beucler and Montagner* (2006). It was shown that for the same variance reduction, a global parameterization of anisotropy including azimuthal anisotropy requires fewer parameters than an isotropic parameterization. This apparent paradox can be explained by the fact that the increase of physical parameters is largely compensated by the smaller number of geographical parameters, i.e. larger scale heterogeneities. Other tests have questioned whether phase data are sensitive enough to detect azimuthal anisotropy (*Larson et al.*, 1998; *Laske et al.*, 1998) and the use of additional polarization data has been proposed.

Most tomographic models agree that down to about 250-300km, the deep structure is closely related to plate tectonics and continental distribution. Figure 5 presents two horizontal cross-sections from the most recent model of *Debayle et al.* (2005), which illustrates and confirms the robust features of

the upper mantle models published so far since *Montagner and Tanimoto* (1991). In the upper mantle depth range around 100km, all plate boundaries are slow: ridges and back-arc areas are slow, shields are fast and seismic velocity in oceanic areas is increasing with the age of the seafloor. Except at few places, it is found that radial anisotropy expressed through the ξ parameter ($\xi = \frac{V_{SH}^2 - V_{SV}^2}{V_{SV}^2}$) is positive, as large as 10% in some oceanic areas and decreases with depth.

The amplitude of SV-wave azimuthal anisotropy (G parameter) presents an average value of about 2% below oceanic areas (Figure 5b). *Montagner* (1994, 2002) noted a good correlation between seismic azimuthal anisotropy and plate velocity directions (primarily for fast moving plates) given by *Minster and Jordan* (1978) or *DeMets et al.* (1990). However, the azimuth of G-parameter can vary significantly as a function of depth. For instance, at shallow depths (down to 60km), the maximum velocity can be parallel to mountain belts or plate boundaries (*Vinnik et al.*, 1991; *Silver*, 1996; *Babuska et al.*, 1998), but orthogonal to them at large depth. This means that, at a given place, the orientation of fast axis is a function of depth, which explains why the interpretation of SKS splitting with a simple model is often difficult.

As depth increases, the amplitude of heterogeneities rapidly decreases, some trends tend to vanish, and some distinctive features come up: most fast ridges are still slow but slow ridges are hardly visible and back-arc regions are no longer systematically slow below 200km. Large portions of fast ridges are offset with respect to their surface signatures. Below 300km of depth (not shown here), high velocity body below the western and the eastern Pacific rim is the most striking feature, which can be related to subducting slabs.

A visual and quantitative comparison of existing models can be found in the REM (Reference Earth Model) web site at the following address: http://mahi.ucsd.edu/Gabi/rem.html

3 Geodynamic applications

The most popular application of large-scale tomographic models is the understanding of mantle convection. Seismic velocity anomalies can be converted, under some assumptions, into temperature anomalies, density anomalies but also into chemical or mineralogical heterogeneities. The application of seismic anisotropy to geodynamics in the upper mantle is straightforward, if we assume that, due to the lattice preferred orientation (LPO) of anisotropic crystals such as olivine (*Christensen and Lundquist*, 1982; *Nicolas et al.*, 1973), the fast-polarization axis of mineralogical assemblages is in the flow plane parallel to the direction of flow. **Figure 6** shows what is expected for the observable pa-

rameters V_S, ξ, G, ψ_G in the case of a simple convective cell with LPO. Radial anisotropy ξ expresses the vertical ($\xi < 1$) or horizontal character ($\xi > 1$) of convective flow, and the azimuthal anisotropy **G**, can be related to the horizontal flow direction. Conversely, the three maps of V_S, ξ, **G**, can be interpreted in terms of convective flow. These 3 pieces of information are necessary to correctly interpret the data. For example, upwellings or downwellings are both characterized by a weak or negative ξ parameter, but a correlative positive or negative δV_S discriminates between these possibilities. By simultaneously inverting at depth for the different azimuthal terms of Rayleigh and Love waves, it is therefore possible to separate the lateral variations in temperature from those induced by the orientation of minerals. Such an interpretation might however be erroneous in water-rich mantle regions where LPO of minerals such as olivine is not simply related to the strain field (e.g. *Jung and Karato*, 2001). We will only present some examples of interesting applications of anisotropy in large scale geodynamics and tectonics. Seismic anisotropy in the mantle primarily reflects the strain field prevailing in the past (frozen-in anisotropy) for shallow layers or present convective processes in deeper layers. Therefore, it makes it possible to map convection in the mantle. It must be noted that, when only the radial anisotropy is retrieved, its interpretation is non unique. A fine layering of the mantle can also generate such a kind of anisotropy, and neglecting the azimuthal anisotropy can bias the amplitude of radial anisotropy and its interpretation.

The uppermost mantle down to 410km is the depth range where the existence of seismic anisotropy is now widely recognized and well documented. Azimuthal variations have been found for body waves and surface waves in different areas of the world. During the last years, the shear wave splitting, primarily for SKS waves was extensively used to study continental deformation, but very few studies using body waves are devoted to oceanic areas. Conversely, global anisotropic upper mantle models have been primarily derived during the last 10 years from surface waves, which are sensitive to structure below oceanic areas in the absence of ocean bottom stations and consequently of dense body wave data. The intercomparison of anisotropic body wave and surface wave data is still in its infancy. However, as shown by *Montagner et al.* (2000), *Vinnik et al.* (2002), *Simons et al.* (2003) such a comparison is providing encouraging results.

3.1 Oceanic plates

Oceans are the areas where plate tectonics applies almost perfectly and this is particularly the case in the largest one, the Pacific plate. **Figure 7** presents 3 vertical cross-sections at two different latitudes, displaying V_{SV} velocity anomalies (**figure 7a**) and the 2 kinds of anisotropy, which can be

retrieved by simultaneous inversion of Rayleigh and Love waves constant $0 - \Psi$ and azimuthal terms of equation (1) from the model of *Montagner* (2002). In **figure 7b**, the equivalent radial anisotropy of the medium, for S-wave expressed through the ξ parameter, is displayed. The maps of **figure 7c** are the distributions of the G-parameter related to the azimuthal variation of SV-wave velocity. The maximum amplitude of G is around 5% and rapidly decreases as depth increases. The distribution of velocity and anisotropy are completely different for these different cross-sections. The thickening of lithosphere with the age of the seafloor is well observed on V_{SV} velocity maps, but lithosphere is much thicker in the northern cross-section. When compared with the cooling half-space model, bathymetry, heat flux and lithospheric thickness flatten with age (see *Ritzwoller et al.*, 2004 for recent results). This flattening is explained by basal reheating, especially in the Central Pacific and the birth of small-scale convection below the lithosphere (*T and Jaupart*, 1994; *Solomatov and Moresi*, 2000).

Radial cross-sections (**Figure 7b**) show that the $\delta\xi = \xi - \xi_{PREM}$ parameter is usually negative and small, where flow is primarily radial (mid-ocean ridges and subduction zones). For the east Pacific Rise, *Gu et al.* (2005) found that a negative radial anisotropy is observed at least down to 300km. Between plate boundaries, oceans display very large areas with a large positive radial anisotropy such as in the Pacific Ocean (*Ekström & Dziewonski*, 1998), characteristic of an overall horizontal flow field. This very large anisotropy in the asthenosphere might be the indication of a strong deformation field at the base of the lithosphere (*Gung et al.*, 2003), corresponding to the upper boundary layer of the convecting mantle (*Anderson and Regan*, 1983; *Montagner*, 1998).

Since convective flow below oceans is dominated by large scale plate motions, the long wavelength anisotropy found in oceanic lithospheric plates and in the underlying asthenosphere, should be similar to the high-resolution anisotropy measured from body waves. Incidentally, one of the first evidences of azimuthal anisotropy was found in the Pacific Ocean by *Hess* (1964) for Pn-waves. So far, there are very few measurements of anisotropy by SKS splitting in the oceans. Due to the lack of seismic stations on the sea floor (with the exception of H2O halfway between Hawaii and California), the only measurements available for SKS were performed in stations located on ocean islands (*Ansel & Nataf*, 1989; *Kuo & Forsyth*, 1992; *Russo & Okal*, 1999; *Wolfe & Silver*, 1998), which are by nature anomalous objects, such as volcanic hotspots, where the strain field is perturbed by the upwelling material and not necessarily representative of the main mantle flow field. SKS splitting was measured during the temporary MELT experiment on the East-Pacific Rise (*Wolfe & Solomon*, 1998) but the orientation of the splitting is in disagreement with the petrological predictions of *Blackman et al.* (1996). *Walker et al.* (2001) presented a first measurement of SKS splitting at H2O, but it is in disagreement with

independent SKS splitting measurements at the same station by *Vinnik et al.* (2002) and with surface wave anisotropy (*Montagner*, 2002).

The large scale azimuthal anisotropy within and below lithosphere in the depth range 100-300km is closely related to plate motions (*Montagner*, 1994; *Ekström*, 2000) and modeled in this framework (*Tommasi et al.*, 1996). Fast moving oceanic plates are zones where the comparison between directions of plate velocities (*Minster & Jordan*, 1978) or NUVEL-1 (*DeMets et al.*, 1990) and directions of $G-$ parameter is the most successful (**Figure 8**). Conversely, such a comparison is more difficult and controversial below plates bearing a large proportion of continents, such as the European-Asian plate, characterized by a very small absolute motion in the hotspot reference frame and probably a large influence of inherited anisotropy.

The map with the G-parameter at 100km (Figure 5) as well as the cross-sections of figure 7c show that the azimuthal anisotropy is very large along spreading ridges with a large asymmetry for the East Pacific rise. The direction of anisotropy is in very good agreement with plate motion, which is also found in all other available models (*Ekström*, 2000; *Smith et al.*, 2004; *Debayle et al.*, 2005). The anisotropy is also large in the middle of the Pacific plate, but a line of very small azimuthal anisotropy almost parallel to the EPR is observed there (see also Figure 2 for synthetic SKS). This linear area of small anisotropy was named Low Anisotropy Channel (LAC) by *Montagner* (2002). When calculating the variation of the amplitude of azimuthal anisotropy as a function of depth, a minimum comes up between 40 and 60Ma age of the seafloor (Figure 9a). The LAC is presumably related either to cracking within the Pacific plate and/or to secondary convection within and below the rigid lithosphere, predicted by numerical and analog experiments and also translated in the V_S velocity structure (*Ritzwoller et al.*, 2004; **Figure 9b**). These new features provide strong constraints on the decoupling between the plate and asthenosphere. The existence and location of these LACs might be related to the current active volcanoes and hotspots (possibly plumes) in Central Pacific. LACs, which are dividing the Pacific Plate into smaller units, might indicate a future reorganization of plates with ridge migrations in the Pacific Ocean. They call for more thorough numerical modelling.

3.2 Continents

Differences in the thickness of high-velocity layer underlying continents as imaged by seismic tomography have fuelled a long debate on the origin of continental roots (*Jordan*, 1975, 1978). Some global tomographic models provide a continental thickness of about 200-250km in agreement with heat-flow analysis or electrical conductivity, but others suggest thicker zones up to 400km.

Seismic anisotropy can provide fundamental information on the structure of continents, their root and the geodynamic processes involved in mountain building and collision between continents (*Vinnik et al.*, 1992; *Silver*, 1996) such as in Central Asia (*Griot et al.*, 1998a,b). Radial anisotropy ξ is usually very heterogeneous below continents in the first 150-200km of depth with positive or negative areas according to geology. But it seems to display a systematic tendency of being positive at larger depth (down to 300km), whereas it is very large in the oceanic lithosphere in the depth range 50-200km and decreases rapidly at larger depths (*Montagner*, 1994). Conversely, radial anisotropy displays a maximum (though smaller than in oceanic lithosphere) below very old continents (such as Siberian and Canadian Shield) in the depth range 200-400km (*Montagner and Tanimoto*, 1991). Seismic anisotropy below continents, sometimes confined to the upper 220km (*Gaherty & Jordan*, 1995) can still be significant below. A more quantitative comparison of radial anisotropy between different continental provinces is presented in *Babuska et al.* (1998), and demonstrates systematic differences according to the tectonic context. The existence of positive large scale radial anisotropy below continents at depth might be a good indicator of the continental root which was largely debated since the presentation of the model of tectosphere by *Jordan* (1975, 1978, 1981). If this maximum of anisotropy is assumed to be related to an intense strain field in this depth range, it might be characteristic of the boundary between continental lithosphere and "normal" upper mantle material. *Gung et al.* (2003) showed that it is possible to reconcile different isotropic tomographic models by taking into account seismic anisotropy. They find that significant radial anisotropy (with $V_{SH} > V_{SV}$) under most cratons in the depth range 250-400km, similar to that found at shallower depths (80-250km) below oceanic basins. Such a result is also in agreement for the Australian continent (*Debayle and Kennett*, 2000; *Simons et al.*, 2002). So, all results seem to show that the root of continents as defined by radial anisotropy is located between 200 and 300km. However, this result is not correlated with a maximum in azimuthal anisotropy in this depth range (*Debayle and Kennett*, 2005): the fast-moving Australian plate seems to be the only continental region with a sufficiently large deformation at its base to be transformed into azimuthal anisotropy. They propose that, for continents other than Australia, weak influence of basal drag on the lithosphere may explain why azimuthal anisotropy is observed only in a layer located in the uppermost 100 km of the mantle. This layer shows a complex organisation of azimuthal anisotropy suggesting a frozen-in origin of deformation, compatible with SKS splitting.

The difference in radial and azimuthal anisotropies between oceans and continents might reflect a difference of coupling between lithosphere and asthenosphere, through the basal drag. The coupling might be weak below most continental roots, in contrast with the Pacific plate, where the coupling

(reflected by plate direction) is the first order effect in the uppermost 200km for young ages, before thermal instabilities take place at the base of the lithosphere, as evidenced by the existence of low anisotropy channels. These results on the difference between oceanic and continental anisotropies are illustrated in **Figure 10**.

3.3 Velocity and Anisotropy in the transition zone

The transition zone plays a key role in mantle dynamics, particularly the 660km-discontinuity which might inhibit the passage of matter between the upper and the lower mantle. Its seismic investigation is made difficult on the global scale by the poor sensitivity of fundamental surface waves in this depth range and by the fact that teleseismic body waves recorded at continental stations from earthquakes primarily occuring along plate boudaries have their turning point below the transition zone. For body waves, many different techniques using SS-precursors (*Shearer*, 1991) or P-to-S converted waves (*Chevrot et al.*, 1999) were used at global scale to investigate the thickness of the transition zone. In spite of some intial controversies, a recent model by *Lawrence and Shearer* (2006) provides a coherent large-scale image of the transition zone thickness.

Whatever the type of data (normal mode, higher modes of surface waves, body waves), an important feature of the transition zone is that, contrarily to the rest of the upper mantle, the upper transition zone is characterized by a large degree 2 pattern (*Masters et al.*, 1982), and to a less extent, a strong degree 6. The degree 2 pattern (as well as degree 6) can be explained by the predominance of a simple large-scale flow pattern characterized by two upwellings in central Pacific Ocean and Eastern Africa and two downwellings in the Western and Eastern Pacific Ocean (*Montagner & Romanowicz*, 1993), proposed initially in the lower mantle (*Busse*, 1983). This scheme was corroborated by the existence, in the upper transition zone, of a slight but significant degree 4 radial anisotropy displayed by *Montagner & Tanimoto* (1991) and *Roult et al.* (1990) in agreement with the prediction of this model. Therefore, the observations of the geographical distributions of degrees 2, 4, 6 in the transition zone are coherent and spatially dependent. *Montagner* (1994) compared these different degrees to the corresponding degrees of the hotspot and slab distribution. In this simple framework, the distribution of plumes (degree 2+6) are merely a consequence of the large scale simple flow in the transition zone. The degree 6 of velocity in the transition zone is well correlated with the distribution of hotspots and might indicate that many mantle plumes might originate in the transition zone. *Ritsema et al.* (2004) observe lower-than-average shear velocity at eight hotspots in this depth range (**Figure 11**). These results suggest that there are different families of plumes, some of them originating in the transition

zone.

As for anisotropy in the transition zone, *Montagner & Kennett* (1996), by using eigenfrequency data, display some evidence of radial anisotropy in the upper (410-660km) and lower (660-900km) transition zones. *Gung and Romanowicz* (2004) also display a slight maximum of the degree 0 ξ in the transition zone. The existence of anisotropy close to the 660km-discontinuity was also found by *Vinnik & Montagner* (1996) below Germany and *Vinnik et al.* (1998) in central Africa. By studying P-to-S converted waves at the GRF network and at GEOSCOPE station BNG in central Africa, they observed that part of the initial P-wave is converted into SH-wave. This signal can be observed on the transverse component of seismograms. The amplitude of this SH-wave cannot be explained by a dipping 660km-discontinuity and it constitutes a good evidence for the existence of anisotropy just above this discontinuity. However, there is some evidence of lateral variation of anisotropy in the transition zone as found by the investigation of several subduction zones (*Fischer & Yang*, 1994; *Fischer & Wiens*, 1996). *Fouch & Fischer* (1996) present a synthesis of these different studies and show that some subduction zones such as Sakhalin Islands require deep anisotropy in the transition zone, whereas others such as Tonga do not need any anisotropy. They conclude that their data might be reconciled by considering the upper transition zone (410-520km) intermittently anisotropic, and the rest of the transition zone might be isotropic.

Anisotropy in the transition zone was also advocated by 2 independent studies, using different datasets. The observations of *Wookey et al.* (2002), though controversial, present evidence of very large S-wave splitting (up to 7.s) in the vicinity of the 660km discontinuity between Tonga-Kermadec subduction zone and Australia. On a global scale, *Trampert and van Heijst* (2002) show a long-wavelength azimuthal anisotropic structure in the transition zone. The rms amplitude of lateral variations of G is about 1%. *Beghein and Trampert* (2003) using probability density functions and separating ξ, ϕ and η anisotropies suggest a chemical component to explain these different parameters. The interpretation of these new tentative results is not obvious and new data are necessary to close the debate on the nature of velocity and anisotropy heterogeneities in the transition zone. The transition zone might be a mid-mantle boundary layer, and a detailed and reliable tomographic model of S-wave velocity and anisotropy in the transition zone will provide fundamental insights into the dynamic of the whole mantle.

4 Numerical Modeling and Perspectives

In the previous sections, we have highlighted the presence of lateral heterogeneities in seismic velocity and anisotropy in different parts of the earth's upper mantle. However, anisotropy is not present in all depth ranges nor at all scales. There is some consensus for the presence of radial anisotropy in many parts of the upper mantle in order to simultaneously explain Love-wave and Rayleigh-wave dispersion and even in the lower mantle (*Panning et al.*, 2004). The existence of azimuthal anisotropy is more controversial, though, from petrological reasons, it turns out that radial anisotropy and azimuthal anisotropy are intimately related and should be searched for simultaneosuly. Additional data such as polarization data might help to provide additional constraints on both kinds of anisotropy (*Yu and Park*, 1993; *Pettersen and Maupin*, 2002). But it requires the development of improved theoretical and numerical methods in order to work on the amplitude of seismograms.

Thanks to the access to very powerful computers, we are at the beginning stage of a new era for seismology. The twentieth century was dominated by the use of ray theory and later on, of normal mode theory. Since it is now feasible to numerically compute synthetic seismograms in complex 3D structures in global spherical geometry (*Komatitsch and Vilotte*, 1998; *Komatitsch and Tromp*, 1999; *Capdeville et al.*, 2003), it is possible to model the complex interaction between seismic waves and 3D heterogeneity, particularly in anisotropic, anelastic media. Some new and sophisticated tomographic methods are presently developed (*Montelli et al.*, 2004; *Capdeville et al.*, 2005; *Tromp et al.*, 2005; *Zhou et al.*, 2006), which should provide access to the complexity of the Earth mantle by the mapping of short-scale heterogeneities such as mantle plumes, in anisotropic and anelastic media.

A second important challenge is the complete understanding of the origin of anisotropy from the mineral scale up to global scale in the different layers of the earth. In the upper mantle, seismic anisotropy is due to LPO of anisotropic minerals such as olivine at large scales, requiring several strong conditions, starting with the presence of anisotropic crystals up to the existence of an efficient large scale present or past strain field. In order to fill the gap between grain scale modeling (*McKenzie*, 1979; *Ribe*, 1989; *Kaminski and Ribe*, 2001) and large scale anisotropy measurements in a convective system (*Tommasi et al.*, 2000), there is now a real need to make more quantitative comparisons between seismic anisotropy and numerical modeling. *Gaboret et al.* (2003) and *Becker et al.* (2003) calculated the convective circulation in the mantle by converting perturbations of S-wave velocity into density perturbations. **Figure 12** shows 2 cross-sections through the Pacific hemisphere and the associated flow lines (*Gaboret et al.*, 2003) derived from the tomographic model of *Ekström and Dziewonski* (1998). This kind of modeling makes it possible to calculate the strain tensor and to test

different hypotheses for the prevailing mechanisms of alignment, by comparison with seismic data.

The upper mantle is the best known of the deep layers of the earth, where there is now good agreement between many isotropic global tomographic models. But the account of seismic anisotropy is mandatory to avoid biased isotropic heterogeneities. The main application of anisotropy is the mapping of mantle convection and of its boundary layers (*Karato*, 1998; *Montagner*, 1998). The finding of anisotropy in the transition zone (if confirmed) will provide strong constraints on the flow circulation and the exchange of matter between the upper and the lower mantle. Pursuing the first pionneering efforts, the systematic modeling of the complete seismic waveform in 3D heterogeneous, anisotropic and anelastic media associated with new techniques of numerical modeling of seismograms will probably enhance our vision of the whole mantle.

In parallel to these theoretical and numerical challenges, there is a crucial need for instrumental developments since there are still many areas at the surface of Earth devoid of broadband seismic stations. These regions are primarily located in southern hemisphere and more particularly in oceanic areas where no islands are present. Therefore, an international effort is ongoing, coordinated through I.O.N. (International Ocean Network) in order to promote the installation of geophysical ocean bottom observatories in order to fill the enormous gaps in the station coverage (for a description of I.O.N., http://seismo.berkeley.edu/seismo/ion).

REFERENCES

Aki K., Richards P.G. 1980 *Quantitative Seismology: Theory and Methods*, W. H. Freeman, San Fransisco.

Anderson D.L. 1961 Elastic wave propagation in layered anisotropic media, *J. Geophys. Res.*, **66**, 2953-2963.

Anderson D.L., Bass J.D. 1984 Mineralogy and composition of the upper mantle, *Geophys. Res. Lett.*, **11**, 637-640.

Anderson D.L., Bass J.D. 1986 Transition region of the Earth's upper mantle, *Nature*, **320**, 321-328.

Anderson D. L., Dziewonski A.M. 1982 Upper mantle anisotropy: Evidence from fre oscillations, *Geophys. J. R. Astron. Soc.*, **69**, 383-404.

Anderson D.L., J. Regan 1983 Upper mantle anisotropy and the oceanic lithosphere, *Geophys. Res. Lett.*, **10**, 841-844.

Ansel V., Nataf H.-C. 1989 Anisotropy beneath 9 stations of the Geoscope broadband network as deduced from shear wave splitting, *Geophys. Res. Lett.*, **16**, 409–412.

Babuska V., Cara M. 1991 Seismic Anisotropy in the Earth, Kluwer Academic Press, Dordrecht, The Netherlands

Babuska V., Montagner J.P., Plomerova J., Girardin N. 1998 Age-dependent large-scale fabric of the mantle lithosphere as derived from surface-wave velocity anisotropy, *Pure Appl. Geophys.*, **151**, 257-280.

Backus G. E., Gilbert F. 1967 Numerical applications of a formalism for geophysical inverse problems, *Geophys. J. R. Astron. Soc.*, **13**, 247-276.

Backus G. E., Gilbert F. 1968 The resolving power of gross earth data, *Geophys. J. R. Astron. Soc.*, **16**, 169-205.

Backus G. E., Gilbert F. 1970 Uniqueness in the inversion of inaccurate gross earth data, *Philos. Trans. R. Soc. London, Ser. A*, **266**, 123-192.

Barmin M.P., Levshin A.L., Ritzwoller M.H. 2001 A fast and reliable method for surface wave tomography, *Pure Appl. Geophys.*, **158**, 1351–1375.

Bass J., Anderson D.L. 1984 Composition of the upper mantle: Geophysical tests of two petrological models, *Geophys. Res. Lett.*, **11**, 237-240.

Becker T.W., Boschi L. 2002 A comparison of tomographic and geodynamic mantle models, *Geochem. Geophys.*, **3**, 2001GC00168.

Becker T.W., Kellog J.B., Ekström G., O'Connell R.J. 2003 Comparison of azimuthal anisotropy from surface waves and finite-strain from global mantle-circulation models, *Geophys. J. Int.*, **155**, 696–714.

Beghein C., Trampert J. 2003 Probability density functions for radial anisotropy: implications for the upper 1200km of the mantle, *Earth Planet. Sci. Lett.*, **217**, 151-162

Beucler E., Montagner J.-P. 2006 Computation of large anisotropic seismic heterogeneities, *Geophys. J. Int.*, in press

Beucler E., Stutzmann E., Montagner J.-P. 2003 Measuring surface wave higher mode velocities by the Roller Coaster Algorithm, *Geophys. J. Int.*, **155**, 289-307.

Blackman D.K., Kendall J.M., Dawson P.R., Wenk H.R., Boyce D., Morgan J.P. 1996 Teleseismic imaging of subaxial flow at mid-ocean ridges: Traveltime effects of anisotropic mineral texture in the mantle, *Geophys. J. Int.*, **127**, 415-426.

Boschi L., Ekström G. 2002 New images of the Earth's upper mantle from measurements of surface wave phase velocity anomalies, *J. Geophys. Res.*, **107**, B4, 10.1029/2000JB000059.

Busse F.H. 1983 Quadrupole convection in the lower mantle, *Geophys. Res. Lett.*, **10**, 285–288.

Capdeville Y., Chaljub E., Vilotte J.-P., Montagner J.-P. 2003 Coupling Spectral Elements and Modal solution: A new efficient tool for numerical wave propagation in laterally Heterogeneous Earth models, *Geophys. J. Int.*, **152**, 34-66.

Capdeville Y., Gung Y., Romanowicz B. 2005 Towards global earth tomography using the spectral element method: a technique based on source stacking, *Geophys. J. Int.*, **162**, 541–554.

Cara M. 1979 Lateral variations of S-velocity in the upper mantle from higher Rayleigh modes, *Geophys. J. R. Astron. Soc.*, **57**, 649–670.

Cara M., Lévêque J.-J. 1988 Anisotropy of the asthenosphere: The higher mode data of the Pacific revisited, *Geophys. Res. Lett.*, **15**, 205-208.

Chevrot S., Vinnik L., Montagner J.-P. 1999 Global-scale analysis of the mantle Pds phase, *J. Geophys. Res.*, **104**, 20,203-20,219.

Chevrot S., Favier, N., Komatitsch D. 2004, Shear wave splitting in three-dimensional anisotropic media, *Geophys. J. Int.*, **159**, 711–720.

Christensen N.I., Lundquist S. 1982 Pyroxene orientation within the upper mantle, *Bull. Geol. Soc. Am.*, **93**, 279-288.

Crampin S. 1984 An introduction to wave propagation in anisotropic media, *Geophys. J. R. Astron. Soc.*, **76**, 17–28.

Dahlen F.A., Hung S.-H., Nolet, G. 2000 Fréchet kernels for finite-frequency traveltimes, I, Theory, *Geophys. J. Int.*, **141**, 157–174.

Davaille A., Jaupart C. 1994 Onset of thermal convection in fluids with temperature-dependent viscosity: Application to the oceanic mantle *J. Geophys. Res.*, **99**, 19,853–19,866.

Debayle E., Lévêque J.-J. 1997 Upper mantle heterogeneities in the Indian Ocean from waveform inversion, *Geophys. Res.*

Lett., **24**, 245-248.

Debayle E., Cara M., Lévêque J.-J. 2001 Seismic evidence for a deeply rooted low velocity anomaly in the upper mantle beneath the northeastern Afro/Arabian continent, *Earth Planet. Sci. Lett.*, **193**, 369-382.

Debayle E., Kennett B.L.N. 2000 Anisotropy in the Australasian upper mantle from Love and Rayleigh waveform inversion, *Earth Planet. Sci. Lett.*, **184**, 339-351.

Debayle E., Sambridge M. 2004 Inversion of massive surface wave datasets: Model construction and resolution assessment, *J. Geophys. Res.*, **109**, B02316, doi:10.1029/2003JB002652.

Debayle E., Kennett B.L.N. 2005 Global azimuthal anisotropy and the unique plate-motion deformation of Australia, *Nature*, **433**, 509-512.

DeMets C., Gordon R.G., Argus D.F., Stein S. 1990 Current plate motions, *Geophys. J. Int.*, **101**, 425-478.

Dost B. 1990 Upper mantle structure under western Europe from fundamental and higher mode surface waves using the NARS array, *Geophys. J; R. Astron. Soc.*, **100**, 131-151.

Dziewonski A. M. 1984 Mapping the lower mantle: Determination of lateral heterogeneity in P velocity up to degree and order 6, *J. Geophys. Res.*, **89**, 5929-5952.

Dziewonski A. M., Anderson D.L. 1981 Preliminary Reference Earth Model, *Phys. Earth Planet. Int.*, **25**, 297–356.

Dziewonski A. M., Woodhouse J.H. 1987 Global images of the Earth's interior, *Science*, **236**, 37-48.

Dziewonski A. M., Chou G., Woodhouse J.H. 1981 Determination of earthquake source parameters from waveform modeling, *J. Geophys. Res.*, **86**, 2825-2852.

Ekström G. 2000 Mapping the lithosphere and asthenosphere with surface waves: lateral structure and anisotropy, *AGU monograph*,Eds Richards et al. **121**, 239-256.

Ekström G., Tromp J., Larson E.W. 1997 Measurements and global models of surface wave propagation, *J. Geophys. Res.*, **102** 8137-8157.

Ekström G., Dziewonski A.M. 1998 The unique anisotropy of the Pacific upper mantle, *Nature*, **394**, 168-172.

Fischer K.M., Wiens D.A. 1996 The depth distribution of mantle anisotropy beneath the Tonga subduction zone, *Earth Planet. Sci. Lett.*, **142**, 253–260.

Fischer K.M., Yang X. 1994 Anisotropy in Kuril-Kamtchatka subduction zone structure, *Geophys. Res. Lett.*, **21**, 5-8.

Forsyth D. W. 1975 The early structural evolution and anisotropy of the oceanic upper mantle, *Geophys. J. R. Astron. Soc.*, **43**, 103-162.

Fouch M.J., Fischer K.M., Parmentier E.M., Wysession M.E., Clarke T.J. 2000 Shear wave splitting, continental keels, patterns of mantle flow, *J. Geophys. Res.*, **105**, 6255-6275.

Fouch M.J., Fischer K.M. 1996 Mantle anisotropy beneath northwest Pacific subduction zones, *J. Geophys. Res.*, **101**, 15,987- 16,002.

Friederich W. 1999 Propagation of seismic shear and surface waves in a laterally heterogeneous mantle by multiple forward scattering, *Geophys. J. Int.*, **136**, 180-204.

Gaboret C., Forte A., Montagner J.-P. 2003 The unique dynamics of the Pacific Hemisphere mantle and its signature on seismic anisotropy, *Earth Planet. Sci. Lett.*, **208**, 219-233.

Gaherty J.B., Jordan T.H. 1995 Lehmann discontinuity as the base of the anisotropic layer beneath continents, *Science*, *268*, 1468- 1471.

Gilbert, F., Excitation of normal modes of the Earth by earthquake sources, *Geophys. J. R. Astron. Soc.*, **22**, 223-226,

1971.

Griot D.-A., Montagner J.P., Tapponnier P. 1998a Surface wave phase velocity and azimuthal anisotropy in Central Asia, *J. Geophys. Res.*, **103** , 21215–21232.

Griot D.-A., Montagner J.P., Tapponnier P. 1998b Heterogeneous versus homogeneous strain in Central Asia, *Geophys. Res. Lett.*, **25**, 1447-1450.

Gu Y.J., Lerner-Lam A., Dziewonski A.M., Ekström G. 2005 Seismic evidence for deep anisotropy beneath the East Pacific Rise, *Earth Planet. Sci. Lett.*, **232**, 259-272.

Gung Y., Panning M., Romanowicz B., 2003 Global anisotropy and the thickness of continents, *Nature*, **422**, 707–711.

Hadiouche O., Jobert N., Montagner J.P. 1989 Anisotropy of the African continent inferred from surface waves, *Phys. Earth Planet. Int.*, *58*, 61–81.

Hess H. 1964 Seismic anisotropy of the uppermost mantle under the oceans, *Nature*, **203**, 629–631.

Ho-Liu P., Montagner J.-P., Kanamori H. 1989 Comparison of iterative back-projection inversion and generalized inversion without blocks: Case studies in Attenuation tomography, *Geophys. J.*, **97**, 19-29.

Jordan T.H. 1975 The continental tectosphere, *Rev. Geophys.*, **13**, 1–12.

Jordan T.H. 1978 Composition and development of the continental tectosphere, *Nature*, **274**, 544-548.

Jordan T.H. 1981 Continents as a chemical boundary layer, *Philos. Trans. R. Soc. London Ser. A*, **301**, 359-373.

Jung H.Y., Karato S.-I. 2001 Water-induced fabric transitions in olivine, it Science, **293** 1460-1462.

Kaminski E., Ribe N.M. 2001 A kinematic model for recrystallization and texture development in olivine polycrystals, *Earth Planet. Sci. Lett.*, **189**, 253-267.

Karato S.-I., Li P. 1993 Diffusive creep in perovskite: Implications for the rheology of the lower mantle, *Science*, **255**, 771-778.

Karato S.-I. 1998 Seismic anisotropy in the deep mantle, boundary layers and geometry of mantle convection, *Pure Appl. Geophys.*, **151**, 565–587.

Komatitsch D., Vilotte J.-P. 1998 The spectral element method: an effective tool to simulate the seismic response of 2D and 3D geological structures, *Bull. Seism. Soc. Am.*, **88**, 368–392.

Komatitsch D., Tromp J. 1999 Introduction of spectral element method for 3-D seismic wave propagation, *Geophys. J. Int.*, **139**, 806–822.

Kuo B.-Y.,Forsyth D.W. 1992 A search for split SKS waveforms in North Atlantic, *Geophys. J. Int.*, **92**, 6421-6436.

Larson E.W.F., Tromp J., Ekstrom G. 1998 Effects of slight anisotropy on surface waves, *Geophys. J. Int.*, **132**, 654-666.

Laske G., Masters G. 1998 Surface-wave polarization data and global anisotropic structure, *Geophys. J. Int.*, **132**, 508-520.

Laske G., Masters G., Reif C. 2001 CRUST2.0- a new global crustal model at 2x2 degrees, http://mahi.ucsd.edu/Gabi/crust2.html (2001)

Lawrence J.F., Shearer P.M. 2006 A global study of transition zone thickness using receiver functions, *J. Geophys. Res.*, **111**, B06307, doi:10.129/2005JB003973.

Lerner-Lam A.L., Jordan T.H. 1983 Earth structure from fundamental and higher-mode waveform analysis, *Geophys. J.R. astr. Soc.*, **75**, 759-797.

Lévêque J.J., Cara M., Rouland D. 1991 Waveform inversion of surface-wave data: a new tool for systematic investigation of upper mantle structures, *Geophys. J. Int.*, **104**, 565-581.

Li X-D, Tanimoto T. 1993 Waveforms of long period body waves in a slightly aspherical earth, *Geophys. J. Int.*, **112**, 92-112

Li X-D, Romanowicz B. 1995 Comparison of global waveform inversions with and without considering cross branch coupling, *Geophys. J. Int.*, **121**, 695-709.

Li X.D., Romanowicz B. 1996 Global mantle shear velocity model developed using nonlinear aymptotic coupling theory, *J. Geophys. Res.*, **101**, 22,245–22, 273.

Love A. E. H. 1927 *A Treatise on the Theory of Elasticity*, 4th edn., Cambridge University Press, 643pp.

Mainprice D.G., Barruol G., Ben Ismail W. 2000 The seismic anisotropy of the Earth's. mantle: From single crystal to polycrystal, in "Earth's Deep Interior: Mineral Physics and Tomography From the Atomic scale to the Global scale, *Geophys. Mon.*, **117**, 237-.

Masters G., Jordan T.H., Silver P.G., Gilbert F. 1982 Aspherical Earth structure from fundamental spheroidal- mode data, *Nature*, **298**, 609-613.

McKenzie D. 1979 Finite deformation during fluid flow, *Geophys. J.R. Astron. Soc.*, **58**, 687-715.

Minster J. B., Jordan T.H. 1978 Present-day plate motions, *J. Geophys. Res.*, **83**, 5331-5354.

Mitchell B. J., Yu G.-K. 1980 Surface wave dispersion, regionalized velocity models and anisotropy of the Pacific crust and upper mantle, *Geophys. J. R. Astron. Soc.*, **63**, 497-514.

Mochizuki E. 1986 The free oscillations of an anisotropic and heterogeneous Earth, *Geophys. J. R. Astron. Soc.*, **86**, 167-176.

Mocquet A., Romanowicz B. 1989 Three-dimensional structure of the upper mantle beneath the Atlantic Ocean inferred from long-period Rayleigh waves. 2. Inversion, *J. Geophys. Res.*, **95**, 67876798,

Montagner J.-P. 1986a First results on the three dimensional structure of the Indian Ocean inferred from long period surface waves, *Geophys. Res. Lett.*, **13**, 315-318.

Montagner J.-P. 1986b Regional three-dimensional structures using long-period surface waves, *Ann. Geophys.*, **4**, B3, 283–294.

Montagner J.-P. 1994 What can seismology tell us about mantle convection? *Rev. Geophys.*,**32,2**, 115-137.

Montagner J.-P. 1998 Where can seismic anisotopy be detected in the Earth's mantle? In boundary layers..., *Pure Appl. Geophys.*, **151**, 223-256.

Montagner J.-P. 2002 upper mantle low anisotropy channels below the Pacific plate *Earth Planet. Sci. Lett.*,**202**, 263-274.

Montagner J.-P., Anderson D.L. 1989a Constraints on elastic combinations inferred from petrological models, *Phys. Earth Planet. Int.*, **54**, 82–105.

Montagner J.-P., Anderson D.L. 1989b Constrained reference mantle model, *Phys. Earth Planet. Int.*, **58**, 205- 227.

Montagner J.-P., Griot D.A., Lavé J. 2000 How to relate body wave and surface wave anisotropies?,*J. Geophys. Res.*, **105**, 19,015–19,027.

Montagner J.-P., Guillot L. 2003 Seismic anisotropy and global geodynamics, *Min. Soc.Am.*, **51**, 353-385.

Montagner J.-P., Jobert N. 1981 Investigation of upper mantle structure under young regions of the Sout-East Pacific using long-period Rayleigh waves, *Phys. Earth Planet. Int.*, **27**, 206-222.

Montagner J.-P., Jobert N. 1988 Vectorial Tomography. II: Application to the Indian Ocean, *Geophys. J.R. astr. Soc.*, **94**, 309–344.

Montagner J.P., Kennett B.L.N. 1996 How to reconcile body-wave and normal-mode reference Earth models? *Geophys. J.*

Int., **125**, 229-248.

Montagner J.-P., Lognonné P., Beauduin R., Roult G., Karczewski J.-F., Stutzmann E. 1998 Towards multiscale and multiparameter networks for the next century: The French efforts, *Phys. Earth Planet. Int.*, **108**, 155-174.

Montagner J.-P., Nataf H.C. 1986 On the inversion of the azimuthal anisotropy of surface waves, *J. Geophys. Res.*, **91**, 511–520.

Montagner J.-P., Nataf H.-C. 1988 Vectorial tomography. I: Theory. *Geophys. J.R. astr. Soc.*, **94**, 295-307.

Montagner J.-P., Tanimoto T. 1990 Global anisotropy in the upper mantle inferred from the regionalization of phase velocities, *J. Geophys. Res.*, **95**, 4797-4819.

Montagner J.-P., Tanimoto T. 1991 Global upper mantle tomography of seismic velocities and anisotropies, *J. Geophys. Res.*, **96**, 20,337–20,351.

Montagner J.-P., Romanowicz B., Karczewski J.F. 1994 A first step towards an Oceanic Geophysical observatory, *EOS, Trans. Am. Geophys. Un.*, **75**, 150-154.

Montagner J.-P., Romanowicz B. 1993 Degrees 2, 4, 6 inferred from seismic tomography, *Geophys. Res. Lett.*, **20**, 631–634,

Montelli R., Nolet G., Dahlen F.A., Masters G., Engdahl R., Hung S. 2004 Finite-frequency tomography reveals a variety of mantle plumes, *Science*, **303**, 338–343.

Mooney W.D., Laske G., Masters G. 1998 CRUST5.1: a global crustal model at 5 x 5, *J. Geophys. Res.*, **96**, 20,337–20,351.

Nataf H.-C., Nakanishi I., Anderson D.L. 1984 Anisotropy and shear velocity heterogeneities in the upper mantle, *Geophys. Res. Lett.*, **11**, 109-112.

Nataf H.-C., Nakanishi I., Anderson D.L. 1986 Measurement of mantle wave velocities and inversion for lateral heterogeneity and anisotropy, III. Inversion, *J. Geophys. Res.*, **91**, 7261-7307.

Nataf H.-C., Ricard Y. 1996 3-SMAC: An a priori tomographic model of the upper mantle based on geophysical modeling, *Phys. Earth Planet. Int.*, **95**, 101-122.

Nicolas A., Boudier F., Boullier A.M. 1973 Mechanisms of flow in naturally and experimentally deformed peridototes, *Am. J. Sci.*, **273**, 853-876.

Nicolas A., Christensen N.I. 1987 Formation of anisotropy in upper mantle peridotites: A review, In "Composition, structure and dynamics of the lithosphere/ Asthenosphere system" (edited by K. Fuchs and C. Froidevaux), American Geophysical Union, Washington D.C., pp. 111-123.

Nishimura C. E., Forsyth D.W. 1989 The anisotropic structure of the upper mantle in the Pacific, *Geophys. J.*, **96**, 203-229.

Nolet G. 1975 Higher Rayleigh modes in Western Europe, *Geophys. Res. Lett.*, **2**, 60-62.

Nolet G., 1990 Partitioned waveform inversion and two-dimensional structure under the network of autonomously recording seismographs, *J. Geophys. Res.*, **95**, 8499-8512.

Okal E., Jo B.-G. 1985 stacking investigation of higher-order mantle Rayleigh waves, *Geophys. Res. Lett.*, **12**, 421-424.

Panning M., Romanowicz B. 2004 Inferences of flow at the base of Earth's mantle based on seismic anisotropy, *Science*, **303**, 351–353.

Park J., Levin V. 2002 Seismic anisotropy: tracing plate dynamics in the mantle, *Science*, **296**, 5567.

Pettersen O., Maupin V. 2002 Lithospheric anisotropy on the Kerguelen hotspot track inferred from Rayleigh wave polarisation anomalies, *Geophys. J. Int.*, **149**, 225-246.

Plomerova J., Sileny J., Babuska V. 1996 Joint interpretation of upper-mantle anisotropy based on teleseismic P-travel time delay and inversion of shear-wave splitting parameters, *Phys. Earth Planet. Int.*, **95**, 293-309

Ribe N.M. 1989 Seismic anisotropy and mantle flow, *J. Geophys. Res.*, **94**, 4213-4223.

Ricard Y., Nataf H.C., Montagner J.-P. 1996 The 3-SMac model: confrontation with seismic data, *J. Geophys. Res.*, **101**, 8457-8472.

Ringwood A.E. 1975 Composition and petrology of the Earth's mantle, McGraw–Hill, New–York, 618pp.

Ritsema J., van Heijst H. J. 2000 Seismic imaging of structural heterogeneity in Earth's mantle: Evidence for large-scale mantle flow, *Sci. Progr.*, **83**, 243-259.

Ritsema J., van Heijst H. J. 2004 Global transition zone tomography, *J. Geophys. Res.*, **109** B02302, doi:10.1029/2003JB002610.

Ritzwoller M.H., Shapiro N.M., Zhong S.-J. 2004 Cooling history of the Pacific lithosphere, *Earth Planet. Sci. Lett.*, **226**, 69-84.

Ritzwoller M.H., Shapiro N.M., Barmin M.P., Levshin A.L. 2002 Global surface wave tomography, *J. Geophys. Res.*, **107** (B12), 2335, 10.1029/2002JB001777.

Romanowicz B. 1987 Multiplet-multiplet coupling due to lateral heterogeneity: asymptotic effects on the amplitude and frequency of the earth's normal modes, *Geophys. J. R. astr. Soc.*, **90**, 75-100.

Romanowicz, B., The upper mantle degree two: Constraints and inferences from global mantle wave attenuation measurements, *J. Geophys. Res.*, **95**, 11,051- 11,071, 1990.

Romanowicz B. 1995 A global tomographic model of shear attenuation in the upper mantle, *J. Geophys. Res..*, **100**, 12375–12394.

Romanowicz B. 2002 Inversion of surface waves: a review, in Handbook of Earthquake and Engineering Seismology, IASPEI, edited by W. H. K. Lee, chap 11, 141- 173.

Romanowicz B. 2003 Global mantle tomography: progress status in the past 10 years, *Ann. Rev. Earth Planet. Sci.*, **31**, 303–328.

Romanowicz B., Cara M., Fels J.-F., Rouland D. 1984 GEOSCOPE: a French initiative in long period, three component, global seismic networks, *EOS, Trans. Am. Geophys. Un.*, **65**, 753-754.

Romanowicz B., Dziewonski A.M. 1986 Towards a Federation of broadband seismic networks, *EOS*, **67**, 541–542.

Romanowicz B., Snieder R. 1988 A new formalism for the effect of lateral heterogeneity on normal modes and surface waves, II: General anisotropic perturbations, *Geophys. J. R. Astron. Soc.*, **93**, 91-99.

Roult G., Rouland D., Montagner J.P. 1994 Antarctica II: Upper mantle structure from velocity and anisotropy, *Phys. Earth Planet. Int.*, **84**, 33-57.

Rumpker G., Silver P.G. 1998 Apparent shear-wave splitting parameters in the presence of vertically varying anisotropy, *Geophys. J. Int.*, **135**, 790-800.

Savage M.K. 1999 Seismic anisotropy and mantle deformation: What have we learned from shear wave splitting?, *Rev. Geophys.*, **37**, 65-106.

Schlue J.W., Knopoff L. 1977 Shear–wave polarization anisotropy in the Pacific Ocean, *Geophys. J.R. astr. Soc.*, **49**, 145–165.

Sebai A., Stutzmann E., Montagner J.-P. 2006 Anisotropic structure of the African upper mantle structure from Rayleigh and Love wave tomography, *Phys. Earth Planet. Int.*, *Phys. Earth Planet. Int.*, **155**, 48–62.

Shapiro N.M., Ritzwoller M.H. 2002 Monte-Carlo inversion for a global shear-velocity model of the crust and upper mantle, *Geophys. J. Int.*, **151**, 88–105.

Shapiro N.M., M. Campillo M., Stehly L., Ritzwoller M.H. 2005 High-resolution surface-wave tomography from ambient

seismic noise, *Science*, **307**, 1615–1618.

Shearer P.M., 1991 Constrains on upper mantle discontinuities from observations of long-period reflected and converted waves, *J. Geophys. Res.*, **96**, 18,147-18,182.

Sicilia D., Montagner J.-P., Cara M., Debayle E., Lepine J.-J., Leveque J.-J. 2005 Shear-wave velocities and anisotropic structure beneath the Afar hotspot, *Earth Planet. Sci. Lett.*, submitted.

Sieminski A., Lévêque J.-J., Debayle E. 2004 Can finite-frequency effects be accounted for in ray theory surface wave tomography, *Geophys. Res. Lett.*, **31**, L24614, doi:10.129/2004GL02142.

Silveira G., Stutzmann E., Montagner J.-P., Mendes-Victor L. 1998 Anisotropic tomography of the Atlantic Ocean from Rayleigh surface waves, *Phys. Earth Planet. Int.*, **106**, 259-275.

Silveira G., Stutzmann E. 2001 Anisotropic tomography of the Atlantic Ocean, *Phys. Earth Planet. Int.*, **132**, 237–248.

Silver P.G. and Savage M. 1994 The interpretation of shear-wave splitting parameters in the presence of two anisotropic layers, *Geophys. J. Int.*, **119**, 949–963.

Silver P.G. 1996 Seismic anisotropy beneath the continents: Probing the depths of geology, *Ann. Rev. Earth Planet. Sci.*, **24**, 385-432.

Silver P.G., Chan W.W. 1988 Implications for continental structure and evolution from seismic anisotropy, *Nature*, **335**, 34–39.

Silver P.G., Holt W.E. 2002 The mantle flow field beneath North America, *Science*, 295, 1054-1057.

Simons F.J., van der Hilst R., Montagner J.P., Zielhuis A. 2002 Multimode Rayleigh wave inversion for shear wave speed heterogeneity and azimuthal anisotropy of the Australian upper mantle, *Geophys. J. Int.*, **151**, 738-754.

Singh S., Taylor M., Montagner J.P. 2000 On the presence of fluids in the Earth 's inner core, *Science*, **287**, 2471-2474.

Smith S.W. 1986 IRIS; a program for the next decade, *EOS, Trans. Am. Geophys. Un.*, **67**, 213-219.

Smith M. L., Dahlen F.A. 1973 The azimuthal dependence of Love and Rayleigh wave propagation in a slightly anisotropic medium, *J. Geophys. Res.*, **78**, 3321-3333.

Smith M. L., Dahlen F.A. 1975 Correction to 'The azimuthal dependence of Love and Rayleigh wave propagation in a slightly anisotropic medium', *J. Geophys. Res.*, **80**, 1923.

Smith D., Ritzwoller M.H, Shapiro, N.M.. 2004 Stratification of anisotropy in the Pacific upper mantle, *J. Geophys. Res.*, **109** , B11309, doi:10.10209/2004JB03200 .

Snieder R. 1988 Large-scale waveform inversions of surface waves for lateral heterogeneity, 1. Theory and numerical examples, *J. Geophys. Res.*, **93**, 12,055–12,066.

Snieder R., Gret A., Douma H., Scales J. 2002 Coda wave interferometry for estimating non-linear behavior in seismic velocity *Science*, **295**, 2253–2255.

Solomatov V.S., Moresi L.N. 2000 Scaling of time-dependent stagnant lid convection: application to small-scale convection on Earth and other terrestrial planets, *J. Geophys. Res.*, **105**, 21795- 21817.

Spetzler J., Trampert J., Snieder R. 2002 The effect of scattering in surface wave tomography, *Geophys. J. Int.*, **149**, 755–767

Stutzmann E., Montagner J.P. 1994 Tomography of the transition zone from the inversion of higher-mode surface waves, *Phys. Earth Planet. Int.*, **86**, 99-116.

Su W.-J., Woodward R.L., Dziewonski A.M. 1984 Degree 12 model of shear velocity heterogeneity in the mantle, *J. Geophys. Res.*, **99**, 6,945–6,980.

Su L., Park J., Yu Y. 1993 Born seismograms using coupled free oscillations: the effect of strong coupling and anisotropy, *Geophys. J. Int.*, **115**, 849-862.

Suetsugu D., Nakanishi I. 1987 Regional and azimuthal dependence of phase velocities of mantle Rayleigh waves in the Pacific Ocean, *Phys. Earth Planet. Int.*, **47**, 230–245.

Suyehiro K., Kanazawa T., Hirata N., Shinohara M., Kinoshita H. 1992 Broadband downhole digital seismometer experiment at site 794: a technical paper, Proc. ODP, Sc. Results, 127-128.

Takeuchi H., Saito M. 1972 Seismic surface waves, in *Methods Comput. Phys.*, **11**, 217-295.

Tanimoto T. 1986 Free oscillations in a slightly anisotropic Earth, *Geophys. J. R. Astron. Soc.*, **87**, 493-517.

Tanimoto T. 1990 Long-wavelength S-wave velocity structure throughout the mantle, *Geophys. J. Int.*, **100**, 327-336, 1990.

Tanimoto T., Anderson D.L. 1985 Lateral heterogeneity and azimuthal anisotropy of the upper mantle: Love and Rayleigh waves 100–250s, *J. Geophys. Res.*, **90**, 1842-1858.

Tarantola A., Valette B. 1982 Generalized nonlinear inverse problems solved using least squares criterion, *Rev. Geophys. Space Phys.*, **20**, 219-232.

Tommasi A., Vauchez A., Russo R. 1996 Seismic anisotropy in ocean basins: Resistive drag of the sublithospheric mantle?, *Geophys.Res. Lett.*, **23**, 2991-2994.

Tommasi A., Mainprice D., Canova G., Chastel Y. 2000 Viscoplastic self-consistent and equilibrium-based modeling of olivine preferred orientations. Implications for the upper mantle anisotropy, J. Geophys. Res., 105, 7893-7908.

Trampert J., Snieder R. 1996 Model estimations biased by truncated expansions: possible artifacts in seismic tomography, *Science*, **271**, 1257–1260.

Trampert J., van Heijst H.J. 2002 Global azimuthal anisotropy in the transition zone, *Science*, **296**, 1297-1299.

Trampert J., Woodhouse J.H. 2003 Global anisotropic phase velocity for fundamental mode surface waves between 40 and 150s, *Geophys. J. Int.*, **154**, 154–165.

Tromp J., Tape C., Liu Q. 2005 Seismic tomography, adjoint methods, time reversal and banana-doughnuts kernels, *Geophys. J. Int.*, **160**, 195–216.

Van Heijst H.J., Woodhouse J.H. 1997 Measuring surface-wave overtone phase velocities using a mode-branch stripping technique, *Geophys. J. Int.*, **131**, 209-230.

Villaseñor A., Ritzwoller M.H., Levshin A.L. , Barmin M.P., Engdahl E.R., Spakman W., Trampert J. 2001 Shear velocity structure of Central Eurasia from inversion of surface wave velocities, *Phys. Earth Planet. Int.*, *123*, 169–184.

Vinnik L.P., Chevrot S., Montagner J.-P. 1998 Seismic evidence of flow at the base of the upper mantle, *Geophys. Res. Lett.*, **25**, 1995-1998.

Vinnik L., Makayeva L.I., Milev A., Usenko A.Y. 1992 Global patterns of azimuthal anisotropy and deformations in the continental mantle, *Geophys. J. Int., 111*, 433-447.

Vinnik L., Montagner J.-P. 1996 Shear wave splitting in the mantle from Ps phases, *Geophys. Res. Lett.*, **23**, 2449- 2452.

Vinnik L., Montagner J.P., Girardin N., Dricker I., Saul J., 2003 Shear wave splitting at H2O: A comment, *Geophys. Res. Lett.*, **30(13)**, 1675, doi:10.1029/2002GL015751.

Walker K.T., Bokelmann G.H., Klemperer S.L. 2001 Shear-wave splitting to test mantle deformation models around Hawaii, *Geophys. Res. Lett.*, **28** , 4319-4322.

Wang Z., Dahlen F.A. 1995 Spherical-spline parameterization of three-dimensinal earth models, *Geophys. Res. Lett.*, **22**, 3099-3102.

Wielandt E., Streickeisen G. 1982 The leaf-spring seismometer: Design and performances, *Bull. Seism. Soc. Am.*, **72**, 2349–2367, 1982.

Wolfe C.J., Silver P.G. 1998 Seismic anisotropy of oceanic upper mantle, *J. Geophys. Res.*, **103**, 749-771.

Wolfe C.J., Solomon S.C. 1998 Shear-wave splitting and implications for mantle flow beneath the Melt region of the East Pacific Rise, *Science*, **280**, 1230-1232.

Woodhouse J. H., Dziewonski A.M. 1984 Mapping the upper mantle: Three dimensional modelling of Earth structure by inversion of seismic waveforms, *J. Geophys. Res.*, **89**, 5953-5986.

Woodhouse J. H., Dahlen F.A. 1978 The effect of a general aspherical perturbation on the free oscillations of the Earth, *Geophys. J. R. Astron. Soc.*, **53**, 335-354.

Wookey J., Kendall J.M., Barruol G. 2002 Mid-mantle deformation inferred from seismic anisotropy, *Nature*, **415**, 777-780.

Yomogida K. 1992 Fresnel-zone inversion for lateral heterogeneities in the Earth, *Pure Appl. Geophys.*, **138**, 391–406.

Yoshizawa K., Kennett B.H.N. 2002 Determination of the influence zone for surface wave paths, *Geophys. J. Int.*, **149**, 441–454.

Yoshizawa K., Kennett B.H.N. 2004 Multimode surface wave tomography for the Australian region using a three-stage approach incorporating finite frequency effects, *J. Geophys. Res.*, **109**, B02310, doi:10,1029/2002JB002254.

Yu Y., Park J. 1993 Anisotropy and coupled long-period surface waves, *Geophys. J. Int.*, **114** , 473-489.

Zhang H., Thurber C.H. 2005 Adaptative mesh seismic tomography based on tetrahedral and Voronoi diagrams: Application to Parkfield, *J. Geophys. Res.*, **110**, B04303, doi:10,129/2004JB003186

Zhang S., Karato S.-I. 1995 lattice preffered orientation of olivines aggregates deformed in simple shear, *Nature*, **375**, 774-777.

Zhou Y., Dahlen F.A., Nolet G. 2004 Three-dimensional sensitivity kernels for surface wave observables, *Geophys. J. Int.*, **158**, 142-168.

Zhou Y., Nolet G., Dahlen F.A., Laske G. 2006 Global upper-mantle structure from finite-frequency surface-wave tomography, *J. Geophys. Res.*, **111**, B04304, doi:10.1029/2005JB003677.

Appendix: Effect of Anisotropy on surface waves in the plane-layered medium

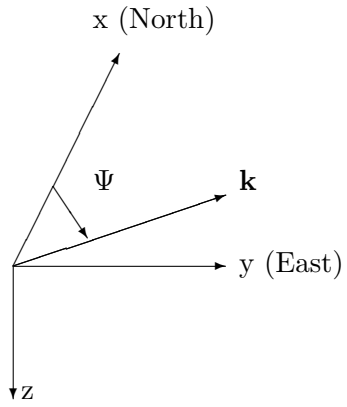

Figure 1: Definition of the Cartesian coordinate system (x, y, z) used in the calculations. Ψ is the azimuth of the wavevector with respect to North.

The half-space is assumed to be homogeneous and may be described by its density $\rho(z)$ and its 4th-order elastic tensor $\Gamma(z)$ with 21 independent elastic coefficients. All these parameters are so far supposed independent of x and y coordinates (z is the vertical component). This condition will be released in the next section. The unperturbed medium is assumed isotropic with an elastic tensor $\Gamma_0(z)$. In that medium, the two cases of Love and Rayleigh wave dispersion can be successively considered.

The unperturbed Love wave displacement is of the form:

$$\mathbf{u}(\mathbf{r},t) = \begin{pmatrix} -W(z)\sin\Psi \\ W(z)\cos\Psi \\ 0 \end{pmatrix} exp(i[k(x\cos\Psi + y\sin\Psi) - \omega t]) \tag{19}$$

where $W(z)$ is the scalar depth eigenfunction for Love waves, k is the horizontal wave number, and Ψ is the azimuth of the wave number k measured clockwise from the North.

The unperturbed Rayleigh wave displacement is of the form:

$$\mathbf{u}(\mathbf{r},t) = \begin{pmatrix} V(z)\cos\Psi \\ V(z)\sin\Psi \\ iU(z) \end{pmatrix} exp(i[k(x\cos\Psi + y\sin\Psi) - \omega t]) \tag{20}$$

where $V(z)$ and $U(z)$ are the scalar depth eigenfunctions for Rayleigh waves. The associated strain tensor $\epsilon(\mathbf{r},t)$ is defined by:

$$\epsilon_{ij}(\mathbf{r},t) = 1/2(u_{i,j} + u_{j,i}) \tag{21}$$

where $,j$ denotes the differentiation with respect to the j-th coordinate. The medium is perturbed from $\Gamma_0(z)$ to $\Gamma_0(z) + \gamma(z)$, where $\gamma(z)$ is small compared to $\Gamma_0(z)$ but quite general in the sense that there is no assumption on the kind of anisotropy. This means that in this approximation, we can still consider quasi-Love modes and quasi-Rayleigh modes (*Crampin*, 1984). From Rayleigh's principle, the first order perturbation $\delta V(\mathbf{k})$ in phase velocity dispersion is (*Smith and Dahlen*, 1973, 1975):

$$\delta V(\mathbf{k}) = \frac{V}{2\omega^2} \frac{\int_0^\infty \gamma_{ijkl}\epsilon_{ij}\epsilon^*_{kl} dz}{\int_0^\infty \rho_0 u_k u^*_k dz} \tag{22}$$

where u_i and ϵ_{ij} are respectively the displacement and the strain for the unperturbed half-space and the asterisk denotes complex conjugation. Now because of the symmetry of the tensors $\gamma(z)$ and ϵ,

we use the simplified index notation c_{ij} and ϵ_i for the elements γ_{ijkl} and ϵ_{ij}, but the number n_{ij} of coefficients γ_{ijkl} for each c_{ij} must be taken into account. The simplified index notation for the elastic tensor γ_{ijkl} is defined in a coordinate system (x_1, x_2, x_3) by:

$$\gamma_{ijkl} \longrightarrow c_{pq} \begin{cases} \text{if } i = j \Rightarrow & p = i \\ \text{if } k = l \Rightarrow & q = k \\ \text{if } i \neq j \Rightarrow & p = 9 - i - j \\ \text{if } k \neq l \Rightarrow & q = 9 - k - l \end{cases} \tag{23}$$

This kind of transformation enables us to relate the 4^{th} order tensor γ (3x3x3x3) to a matrix c (6x6). The same simplified index notation can be applied to the components of the strain tensor ϵ_{ij}, transforming the 2^{nd} order tensor ϵ (3x3) into a vector with 6 components. However, it is necessary to be careful, because to a given c_{pq} correspond several γ_{ijkl}, and γ_{ijkl} must be replaced by $n_{pq}c_{pq}$, where n_{pq} is the number of γ_{ijkl} giving the same c_{pq}. Therefore, the equation (22) expressing Rayleigh's principle can be rewritten as:

$$\delta V(\mathbf{k}) = \frac{V}{2\omega^2} \frac{\int_0^\infty \sum_{ij} n_{ij} c_{ij} \epsilon_i \epsilon_j^* }{\int_0^\infty \rho_0 u_k u_k^* dz} dz \tag{24}$$

We only detail the calculations for Love waves.

• Love waves.

By using previous expressions for $\mathbf{u}(\mathbf{r}, t)$ (19) and $\epsilon_{ij}(\mathbf{r}, t)$ (21), the various expressions of strain are:

$$\begin{cases} \epsilon_1 &= -i \cos\Psi \sin\Psi \, kW \\ \epsilon_2 &= i \cos\Psi \sin\Psi \, kW \\ \epsilon_3 &= 0 \\ \epsilon_4 &= 1/2 \cos\Psi \, W' \\ \epsilon_5 &= -1/2 \sin\Psi \, W' \\ \epsilon_6 &= 1/2(\cos^2\Psi - \sin^2\Psi) \, kW \end{cases} \tag{25}$$

where $W' = \frac{dW}{dr}$. In table 1, the different terms $n_{ij} c_{ij} \epsilon_i \epsilon_j^*$ are given. We note that when $c_{ij}\epsilon_i\epsilon_j^*$ is a purely imaginary complex, its contribution to $\delta V(k, \Psi)$ is null. When all the contributions are summed, the different terms $\cos^k\Psi \sin^l\Psi$ are such that $k + l$ is even, which is not surprising in the light of the reciprocity principle. Therefore, each term can be developed as a Fourier series in Ψ with only even terms. Finally it is found:

$$\begin{aligned} \delta V_L(k, \Psi) \quad = \tfrac{V}{2\omega^2 L_0} \quad & \int_0^\infty dz \{ k^2 W^2 [\frac{1}{8}(c_{11} + c_{22} - 2c_{12} + 4c_{66}] + W'^2 [\frac{1}{2}(c_{44} + c_{55})] \\ & + \cos 2\Psi \, W'^2 [\frac{1}{2}(c_{44} - c_{55})] - \sin 2\Psi \, W'^2 c_{45} \\ & - \cos 4\Psi \, k^2 W^2 [\frac{1}{8}(c_{11} + c_{22} - 2c_{12} - 4c_{66})] \\ & + \sin 4\Psi \, k^2 W^2 [\frac{1}{2}(c_{26} - c_{16})] \} \end{aligned} \tag{26}$$

In the particular case of a transversely isotropic medium with a vertical symmetry axis (also named radial anisotropic medium), we have: $c_{11} = c_{22} = \delta A$, $c_{33} = \delta C$, $c_{12} = \delta(A - 2N)$, $c_{13} = c_{23} = \delta F$, $c_{44} = c_{55} = \delta L$, $c_{66} = \delta N$ and $c_{14} = c_{24} = c_{15} = c_{25} = c_{16} = c_{26} = 0$. The local azimuthal terms vanish and the previous equation (26) reduces to:

$$\delta V_L(k, \Psi) = \frac{1}{2V_L L_0} \int_0^\infty \{ W^2 \delta N + \frac{W'^2}{k^2} \delta L \} dz \tag{27}$$

Therefore, the same expressions as in *Takeuchi and Saito* (1972, p. 268) are found in the case of radial anisotropy. The $0 - \Psi$ term of equation (26) corresponds to the averaging over azimuth Ψ, which provides the equivalent transversely isotropic model with vertical symmetry axis by setting:
$\delta N = \frac{1}{8}(c_{11} + c_{22}) - \frac{1}{4}c_{12} + \frac{1}{2}c_{66}$
$\delta L = \frac{1}{2}(c_{44} + c_{55})$
If we call C_{ij} the elastic coefficients of the total elastic tensor, we can set:

$$N = \rho V_{SH}^2 = \frac{1}{8}(C_{11} + C_{22}) - \frac{1}{4}C_{12} + \frac{1}{2}C_{66}$$

$$L = \rho V_{SV}^2 = \frac{1}{2}(C_{44} + C_{55})$$

According to equation (26), the first order perturbation in Love wave phase velocity $\delta V_L(k, \Psi)$ can then be expressed as:

$$\delta V_L(k, \Psi) = \frac{1}{2V_{0_L}(k)}[L_1(k) + L_2(k)\cos 2\Psi + L_3(k)\sin 2\Psi + L_4(k)\cos 4\Psi + L_5(k)\sin 4\Psi \qquad (28)$$

where

$$\begin{aligned}
L_0(k) &= \textstyle\int_0^\infty \rho W^2 dz \\
L_1(k) &= \tfrac{1}{L_0}\textstyle\int_0^\infty (W^2\delta N + \tfrac{W'^2}{k^2}\delta L)dz \\
L_2(k) &= \tfrac{1}{L_0}\textstyle\int_0^\infty -G_c(\tfrac{W'^2}{k^2})dz \\
L_3(k) &= \tfrac{1}{L_0}\textstyle\int_0^\infty -G_s(\tfrac{W'^2}{k^2})dz \\
L_4(k) &= \tfrac{1}{L_0}\textstyle\int_0^\infty -E_c.W^2 dz \\
L_5(k) &= \tfrac{1}{L_0}\textstyle\int_0^\infty -E_s.W^2 dz
\end{aligned}$$

• Rayleigh waves.
The same procedure holds for the local Rayleigh wave phase velocity perturbation δV_R, starting from the displacement given previously (*Montagner and Nataf*, 1986).

$$\delta V_R(k, \Psi) = \frac{1}{2V_{0_R}(k)}[R_1(k) + R_2(k)\cos 2\Psi + R_3(k)\sin 2\Psi + R_4(k)\cos 4\Psi + R_5(k)\sin 4\Psi \qquad (29)$$

where

$$\begin{aligned}
R_0(k) &= \textstyle\int_0^\infty \rho(U^2 + V^2)dz \\
R_1(k) &= \tfrac{1}{R_0}\textstyle\int_0^\infty [V^2.\delta A + \tfrac{U'^2}{k^2}.\delta C + \tfrac{2U'V}{k}.\delta F + (\tfrac{V'}{k} - U)^2.\delta L]dz \\
R_2(k) &= \tfrac{1}{R_0}\textstyle\int_0^\infty [V^2.B_c + \tfrac{2U'V}{k}.H_c + (\tfrac{V'}{k} - U)^2.G_c]dz \\
R_3(k) &= \tfrac{1}{R_0}\textstyle\int_0^\infty [V^2.B_s + \tfrac{2U'V}{k}.H_s + (\tfrac{V'}{k} - U)^2.G_s]dz \\
R_4(k) &= \tfrac{1}{R_0}\textstyle\int_0^\infty E_c.V^2 dz \\
R_5(k) &= \tfrac{1}{R_0}\textstyle\int_0^\infty E_s.V^2 dz
\end{aligned}$$

The 13 depth-dependent parameters $A, C, F, L, N, B_c, B_s, H_c, H_s, G_c, G_s, E_c, E_s$ are linear combinations of the elastic coefficients C_{ij} and are explicitly given as follows:

Constant term (0 Ψ -azimuthal term: independent of azimuth)

$A = \rho V_{PH}^2 = \frac{3}{8}(C_{11} + C_{22}) + \frac{1}{4}C_{12} + \frac{1}{2}C_{66}$
$C = \rho V_{PV}^2 = C_{33}$
$F = \frac{1}{2}(C_{13} + C_{23})$

$L = \rho V_{SV}^2 = \frac{1}{2}(C_{44} + C_{55})$
$N = \rho V_{SH}^2 = \frac{1}{8}(C_{11} + C_{22}) - \frac{1}{4}C_{12} + \frac{1}{2}C_{66}$

2 Ψ -azimuthal term:

$\cos 2\Psi$	$\sin 2\Psi$
$B_c = \frac{1}{2}(C_{11} - C_{22})$	$B_s = C_{16} + C_{26}$
$G_c = \frac{1}{2}(C_{55} - C_{44})$	$G_s = C_{54}$
$H_c = \frac{1}{2}(C_{13} - C_{23})$	$H_s = C_{36}$

4 Ψ -azimuthal term:

$\cos 4\Psi$	$\sin 4\Psi$
$E_c = \frac{1}{8}(C_{11} + C_{22}) - \frac{1}{4}C_{12} - \frac{1}{2}C_{66}$	$E_s = \frac{1}{2}(C_{16} - C_{26})$

where indices 1 and 2 refer to horizontal coordinates (1: North; 2: East) and index 3 refers to vertical coordinate. ρ is the density, V_{PH}, V_{PV} are respectively horizontal and vertical propagating P-wave velocities, V_{SH}, V_{SV} horizontal and vertical polarized S-wave velocities. We must bear in mind that A, C, L, N anisotropic parameters can be retrieved from measurements of the P- and S- wave velocities propagating perpendicular or parallel to the axis of symmetry.

Table 1: Calculation of the various $c_{ij}\epsilon_i\epsilon_j$ for Love waves, with the simplified index notation. $\alpha = \cos\Psi$; $\beta = \sin\Psi$

n	ij	$c_{ij}\epsilon_i\epsilon_j$
1	11	$c_{11}\alpha^2\beta^2.k^2W^2$
1	22	$c_{22}\alpha^2\beta^2.k^2W^2$
1	33	0
2	12	$-c_{12}\alpha^2\beta^2.k^2W^2$
2	13	0
2	23	0
2	24	0
4	14	$c_{14}(-i\alpha^2\beta).\frac{kWW'}{2}$
4	15	$c_{15}(i\alpha^2\beta).\frac{kWW'}{2}$
4	16	$c_{16}(-\alpha\beta)(\alpha^2-\beta^2).\frac{k^2W^2}{2}$
4	24	$c_{24}(-i\alpha^2\beta).\frac{kWW'}{2}$
4	25	$c_{25}(-i\alpha\beta^2).\frac{kWW'}{2}$
4	26	$c_{26}(\alpha\beta)(\alpha^2-\beta^2).\frac{k^2W^2}{2}$
4	34	0
4	35	0
4	36	0
4	44	$c_{44}\alpha^2.\frac{W'^2}{4}$
8	45	$c_{45}(-\alpha\beta).\frac{W'^2}{4}$
8	46	$c_{46}(-i\alpha)(\alpha^2-\beta^2).\frac{kWW'}{2}$
4	55	$c_{55}\beta^2.\frac{W'^2}{4}$
8	56	$c_{56}(i\beta)(\alpha^2-\beta^2).\frac{kWW'}{2}$
4	66	$c_{66}(\alpha^2-\beta^2).\frac{k^2W^2}{4}$

Acknowledgments. I would like to thank Barbara Romanowicz and an anonymous reviewer for constructive reviews, as well as my colleagues from IPG of Paris

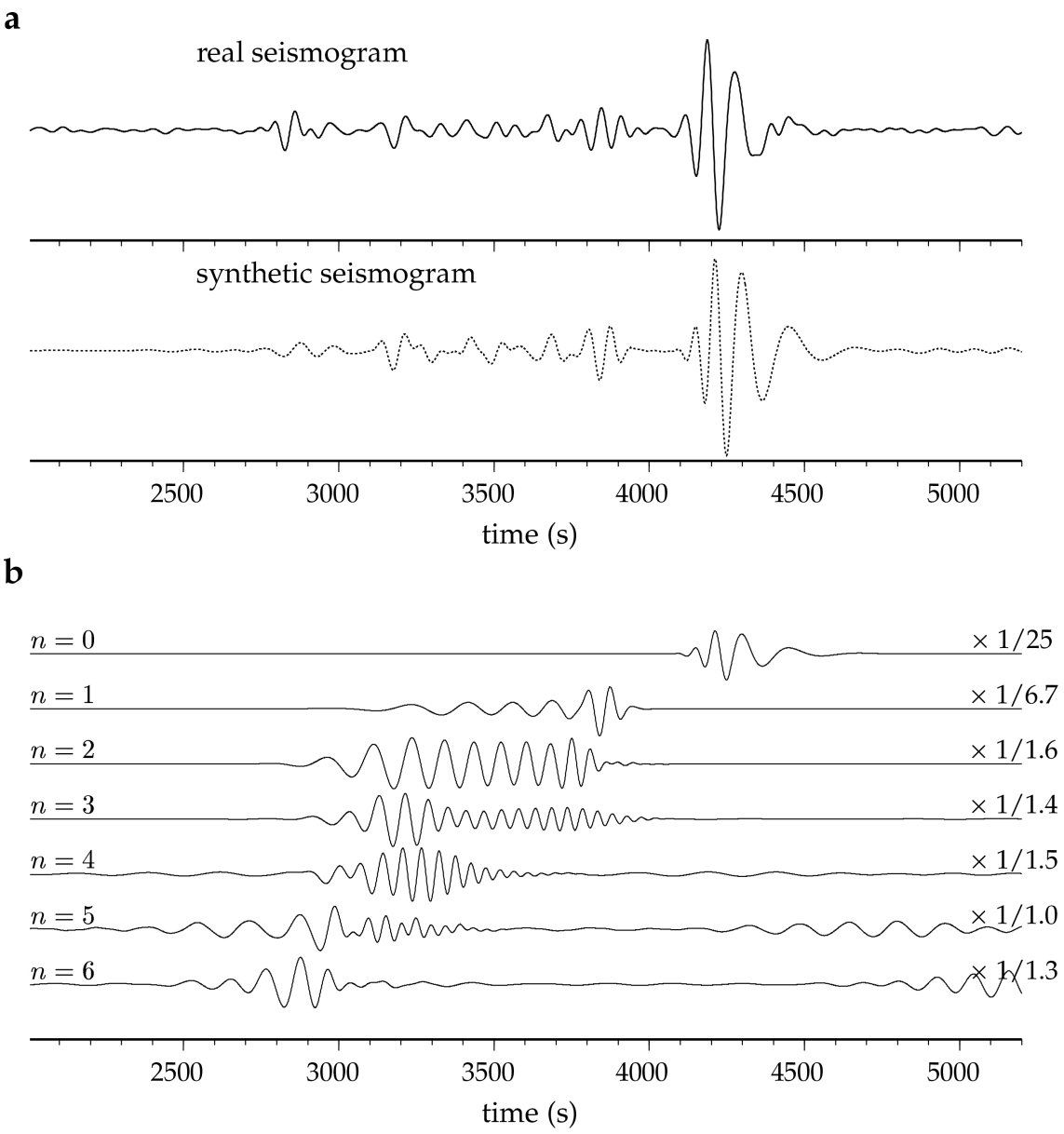

Figure 1 : example of real and synthetic seismograms used for retrieving Rayleigh wave dispersion curve for the fundamental mode and overtones (Beucler et al., 2003). Behind body waves, the signal is composed of surface waves. The complex phase before the high amplitude wave packet corresponding to the fundamental mode of Rayleigh wave (n=0) can be synthetized by summing the first overtones.

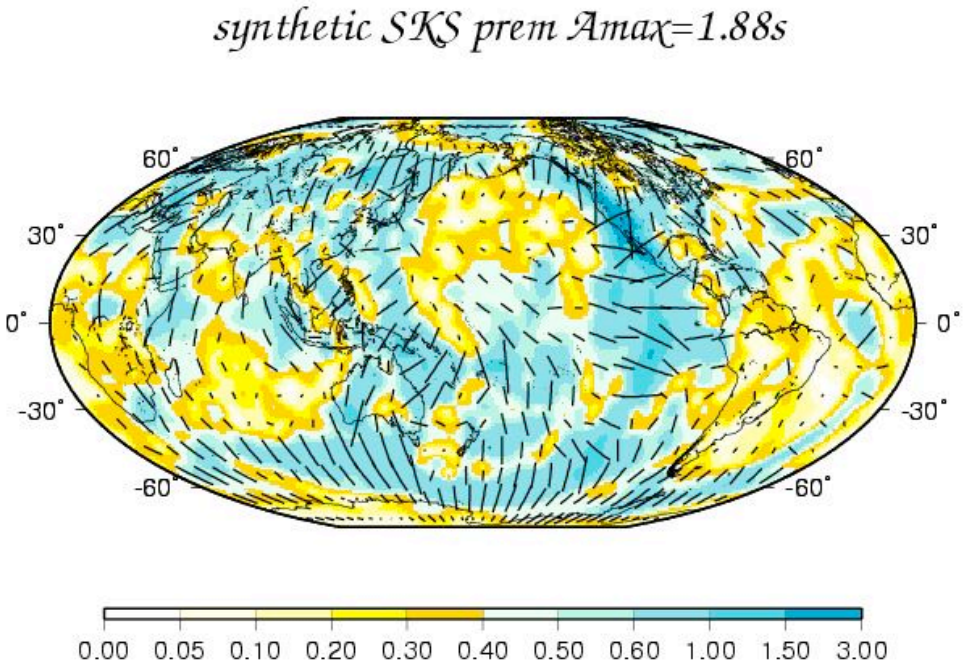

Figure 2 : Map of synthetic SKS splitting derived from the anisotropic surface wave model of Montagner (2002). The delay time is expressed in seconds.

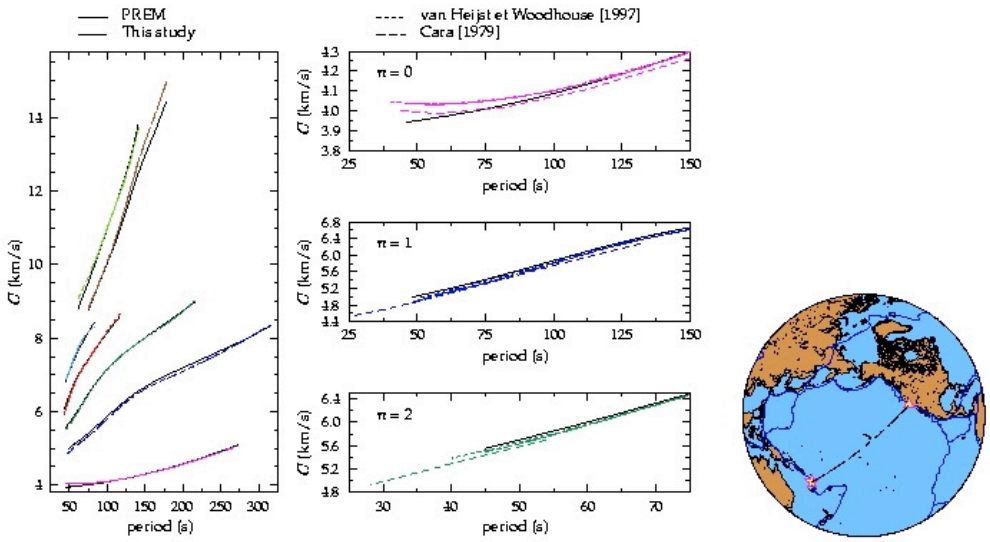

Comparison with previous results along the Vanuatu-California path.

Figure 3 : Phase velocity of the fundamental mode and the first 6 higher modes of Rayleigh compared with PREM (right plot) and with results (center) obtained in previous studies along the same path between Vanuatu and California (SCZ Geoscope station) (Beucler et al., 2003).

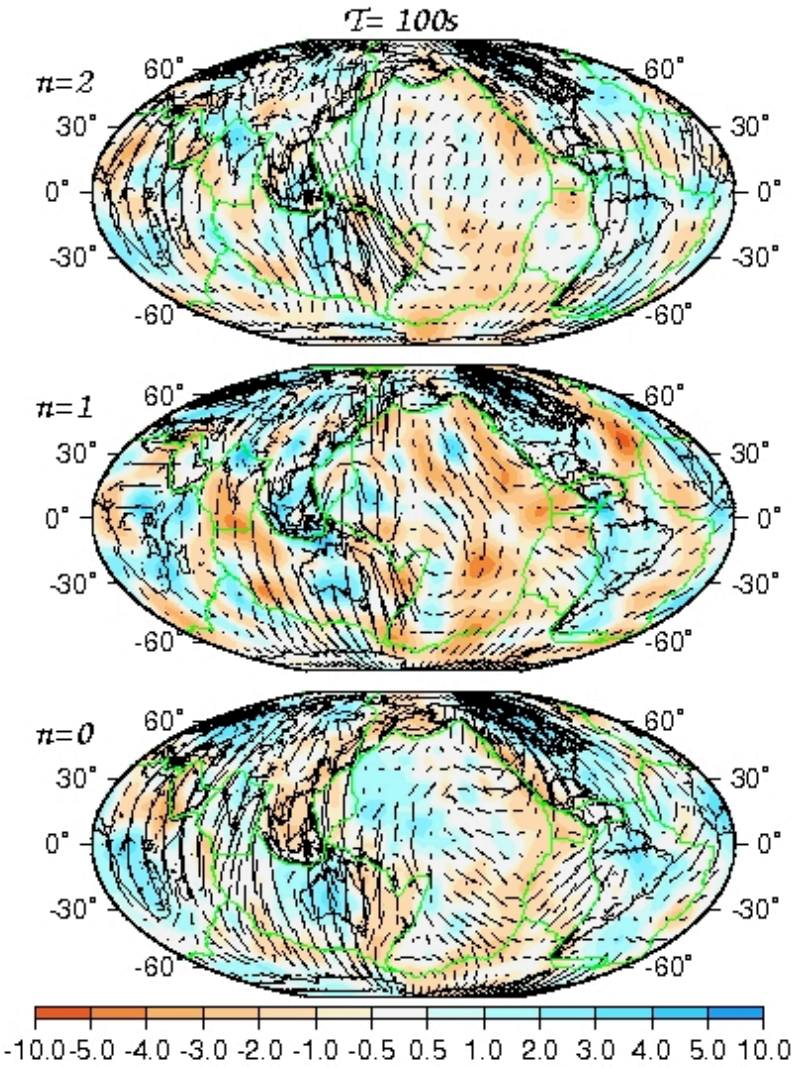

Figure 4 : Rayleigh wave Phase velocity maps at period T=100S for the first 3 modes (n=0, 1, 2) after Beucler and Montagner (2006)

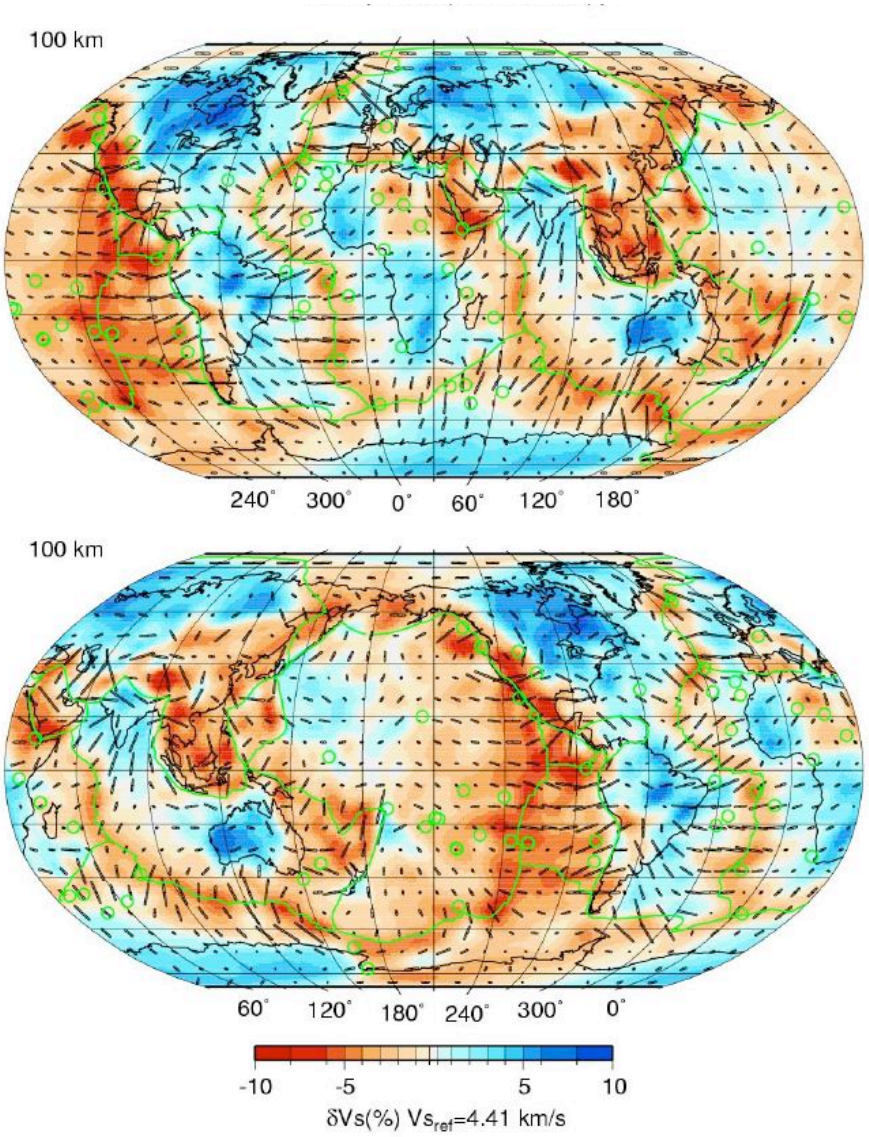
100 km
240° 300° 0° 60° 120° 180°
100 km
60° 120° 180° 240° 300° 0°
-10 -5 5 10
δVs(%) Vs$_{ref}$=4.41 km/s

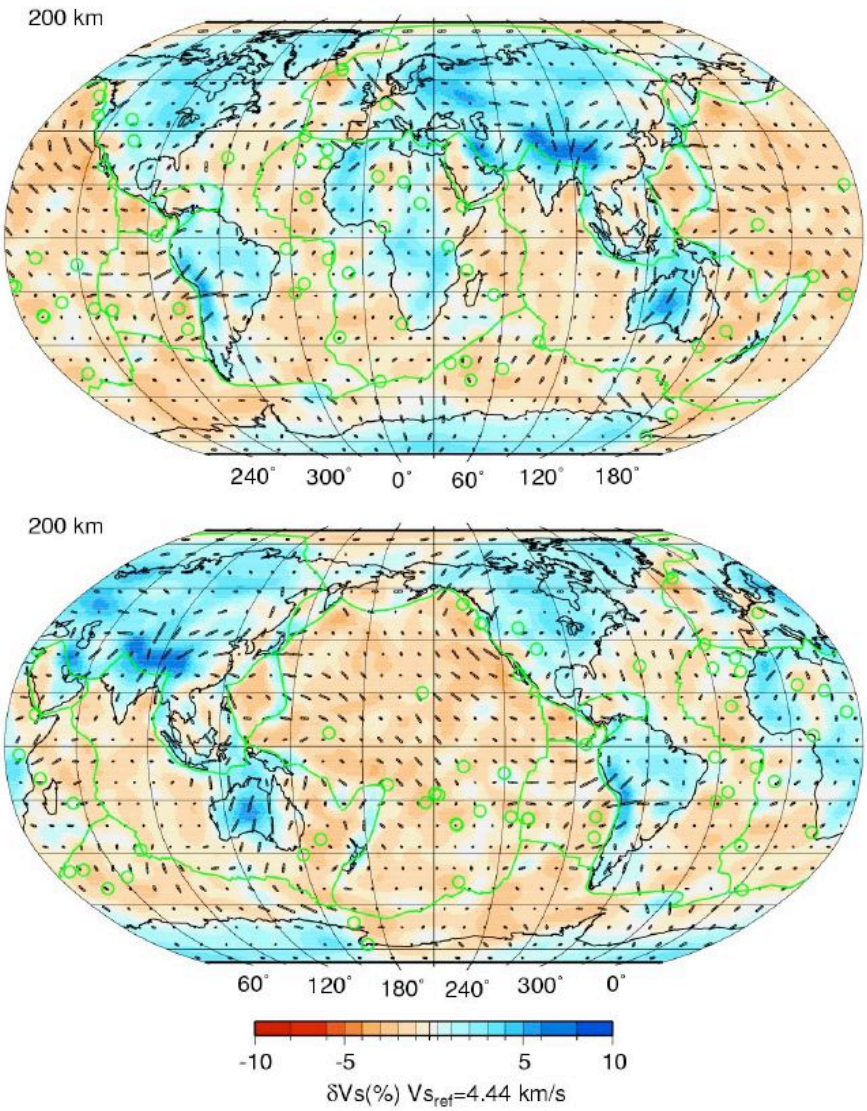

Figure 5 : 2 cross-sections at 100km (top) and 200km (bottom) depths of the global tomographic model of Debayle et al. (2005). Directions of azimuthal anisotropy are superimposed on S-wave velocity heterogeneities. The length of bars is proportional to its amplitude (<2%)

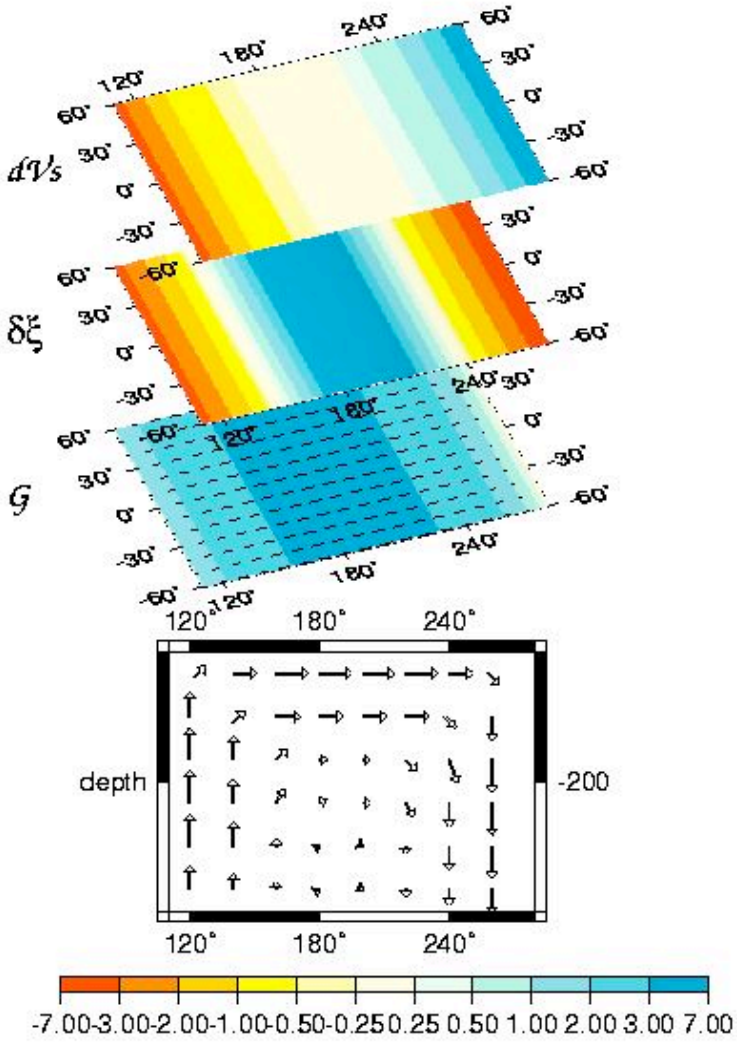

Figure 6 : The seismic observable parameters V_S, ξ, G, Ψ_G associated with a simple convecting cell in the upper mantle, assuming lattice-preferred orientation of anisotropic minerals such as olivine. A vertical flow is characterized by a negative ξ radial anisotropy (ratio between V_{SH} and V_{SV} and a small azimuthal anisotropy (G≈ 0). An upwelling (resp. downwelling) is characterized by a large positive (resp. negative) temperature anomaly inducing δV_S <0 (resp. δV_S >0).
A predominant large scale horizontal flow will be translated into a significant amplitude of the G azimuthal anisotropy and its orientation will reflect the direction of flow (with a 180° ambiguity)
(After Montagner, 2002).

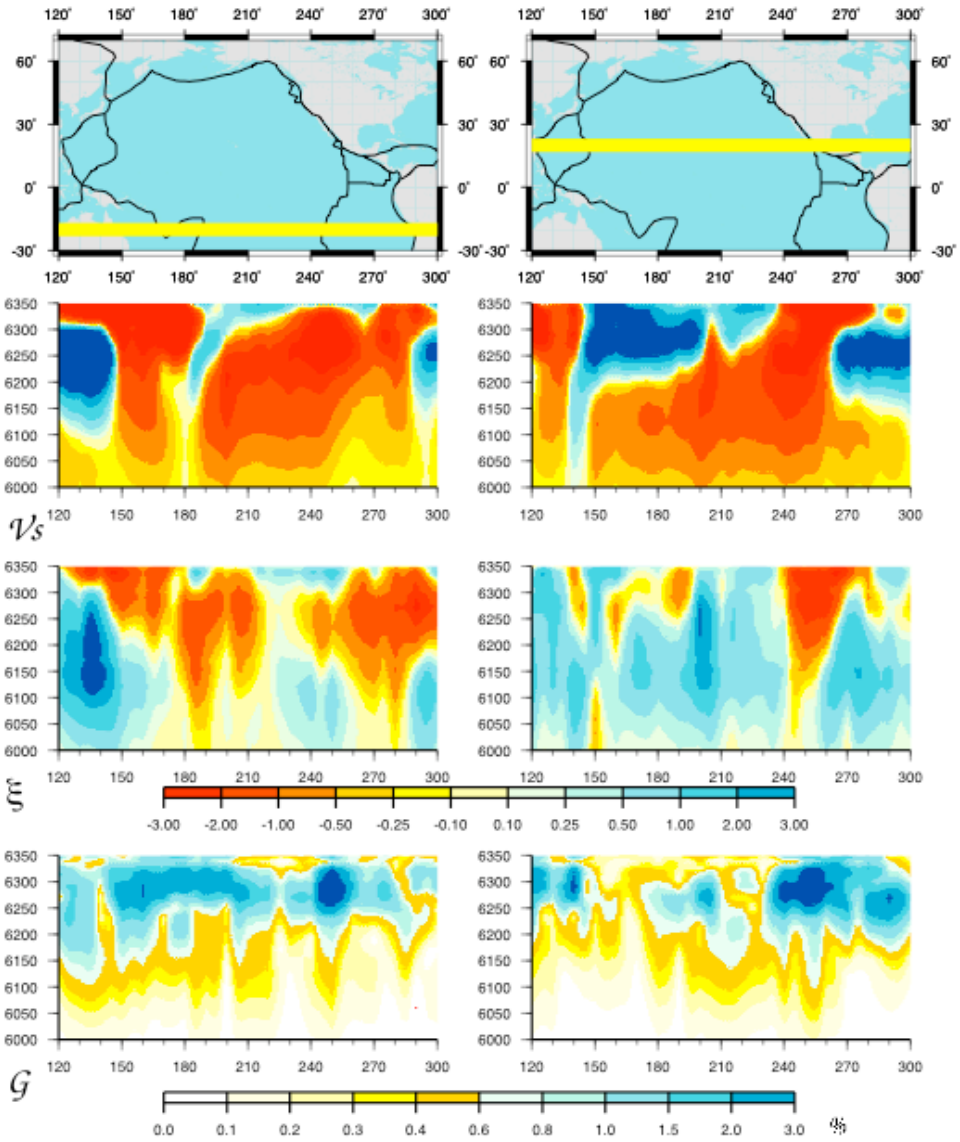

Figure 7: Vertical cross-sections of the distribution of V_S, $\xi-\xi_{ref}$, G in the Pacific Plate at –20° south and 20° north between radii 6000km (370kmdepth) and 6350km (20km depth) (after *Montagner*, 2002). The color scales in percents are the same for V_S and ξ.

The vertical scale is exaggerated to make the figures more readible.

a) V_S $ V_S$

b) $\delta \xi = \xi-\xi_{ref}$: deviation of ξ with respect to a reference model (ξ_{ref} PREM model)

c) G : amplitude of azimuthal anisotropy- parameters

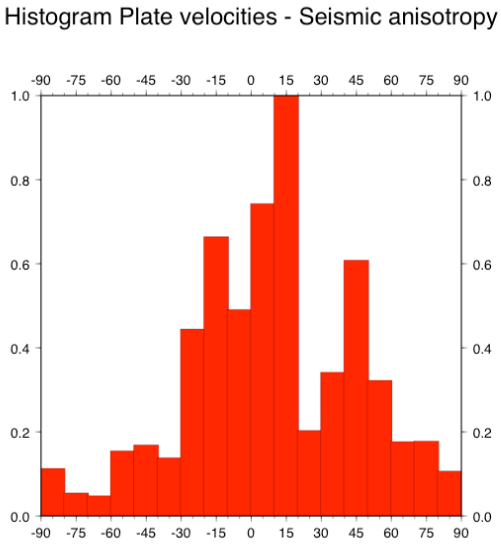

Figure 8 : Histogram of the difference between plate velocities directions and synthetic SKS anisotropy azimuths in the Pacific plate (After Montagner, 2002). It is calculated by summing the contributions of each grid point (5°x5°) weighted by the latitude and the amplitude of anisotropy.

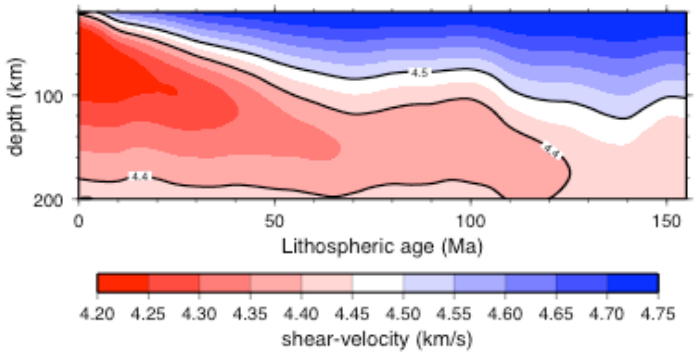

Fig. 9a Average shear velocity structure (After Ritzwoller et al., 2004)

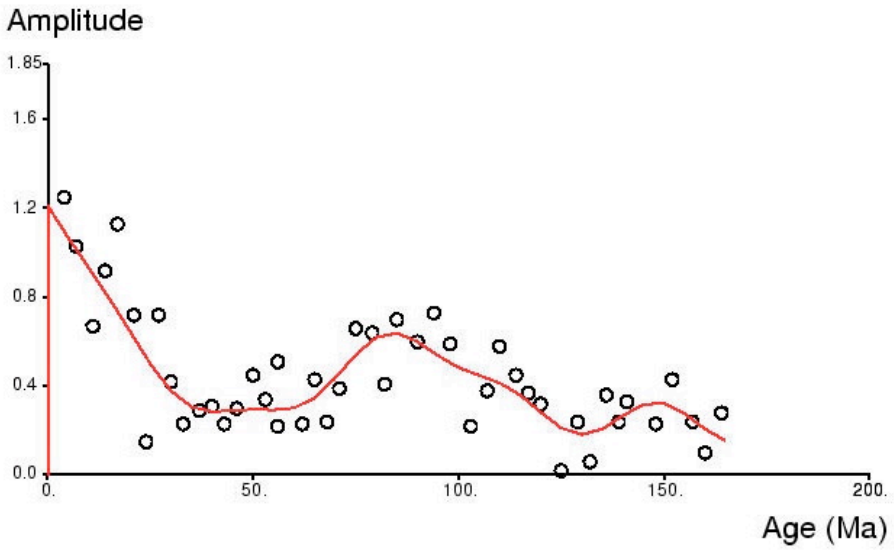

Fig 9b Azimuthal delay time in seconds (After Montagner, 2002)

Figure 9 : variations of average S-wave velocity and azimuthal anisotropy (through the delay time of synthetic SKS splitting) plotted versus the age of lithosphericsea floor. In both cases the structure below the plate for age between 60 to 100Ma looks anomalous.

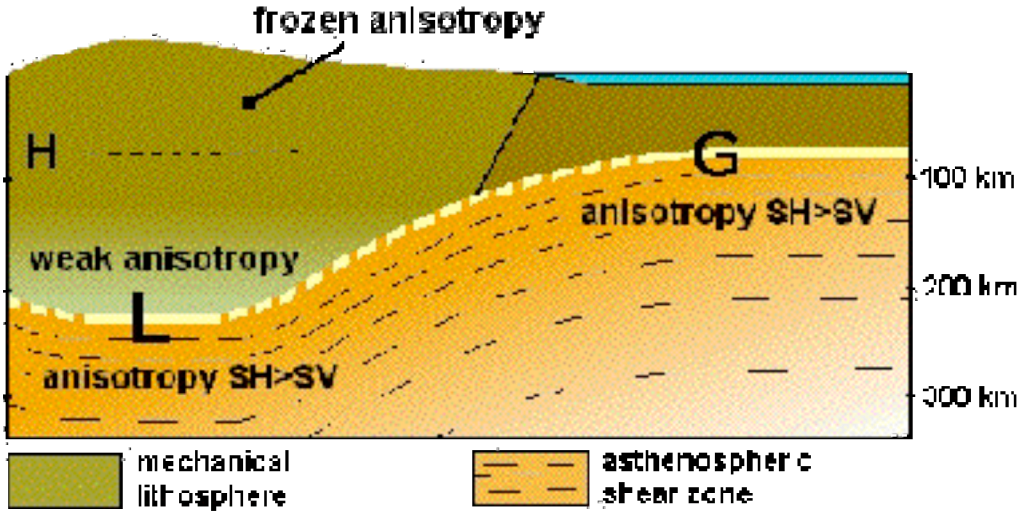

Figure 10 : Scheme illustrating the difference in the location of maximum anisotropy between oceans and continents.
Adapted from Gung et al. (2003).

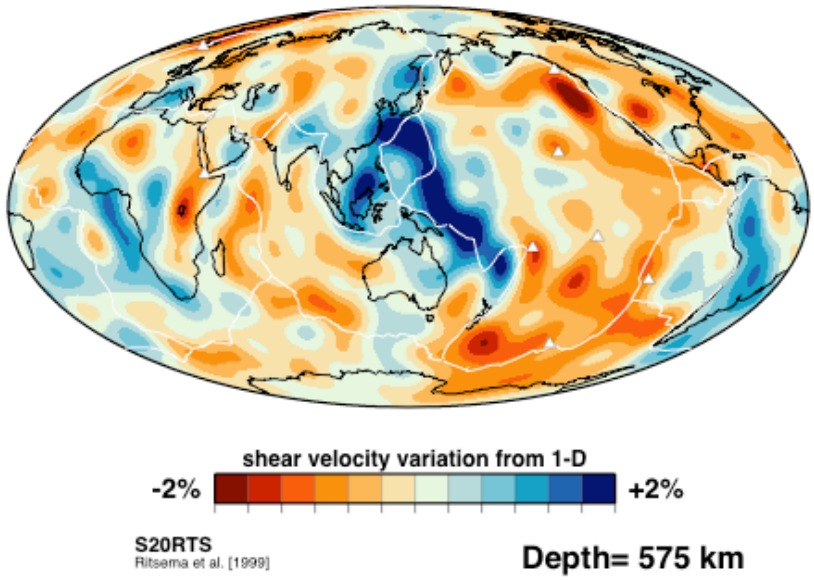

Figure 11: Transition zone Heterogeneities
Model of shear velocity in the transition zone at 575km depth derived by inverting fundamental-mode and overtone Rayleigh wave phase velocoties, and teleseismic body wave data (from Ritsema et al., 2004).

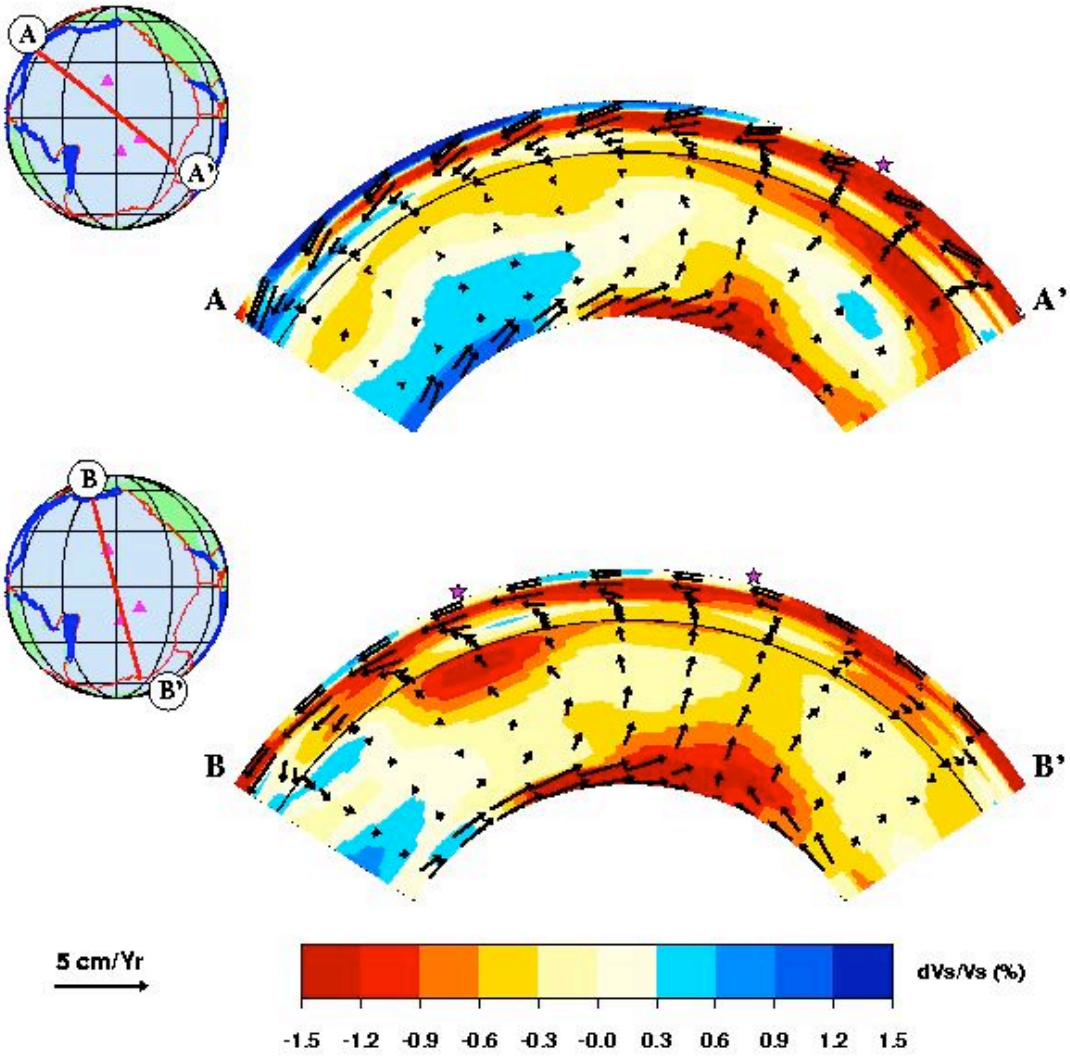

Figure 12 :Mantle heterogeneities and convective flow below the Pacific Ocean. Adapted from Gaboret et al. (2003)

Figure A1 : Definition of the Cartesian coordinate system (x,y,z) used in the calculations. Y is the azimuth of the wavevector with respect to North.

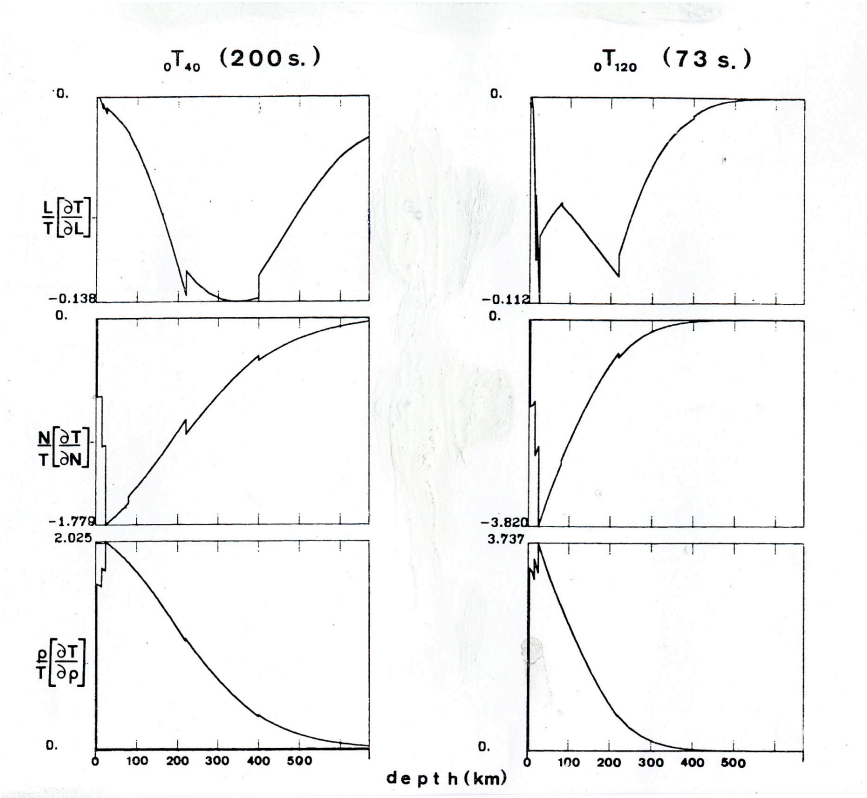

Figure A2 : Partial derivatives for Love waves of the period of fundamental normal modes 0T40 (left) and 0T120 (right) with respect to the elastic coefficients of a transversely isotropic earth L, N and density ρ, as a function of depth in the upper mantle (from Montagner and nataf, 1986). The partial derivatives with respect to A, C, F are null for these modes. The plots are normalized to their maximum amplitudes, given for a Δh=1000km thick perturbed layer. The combinations of elastic coefficients that have the same partial derivative as L are $-G_c$, $-G_s$ for the azimuthal terms 2Ψ, and as N are E_c, E_s for the azimuthal term 4Ψ. Note that the amplitude of the L-partial is very small for the fundamental modes, which is not the case for higher modes.

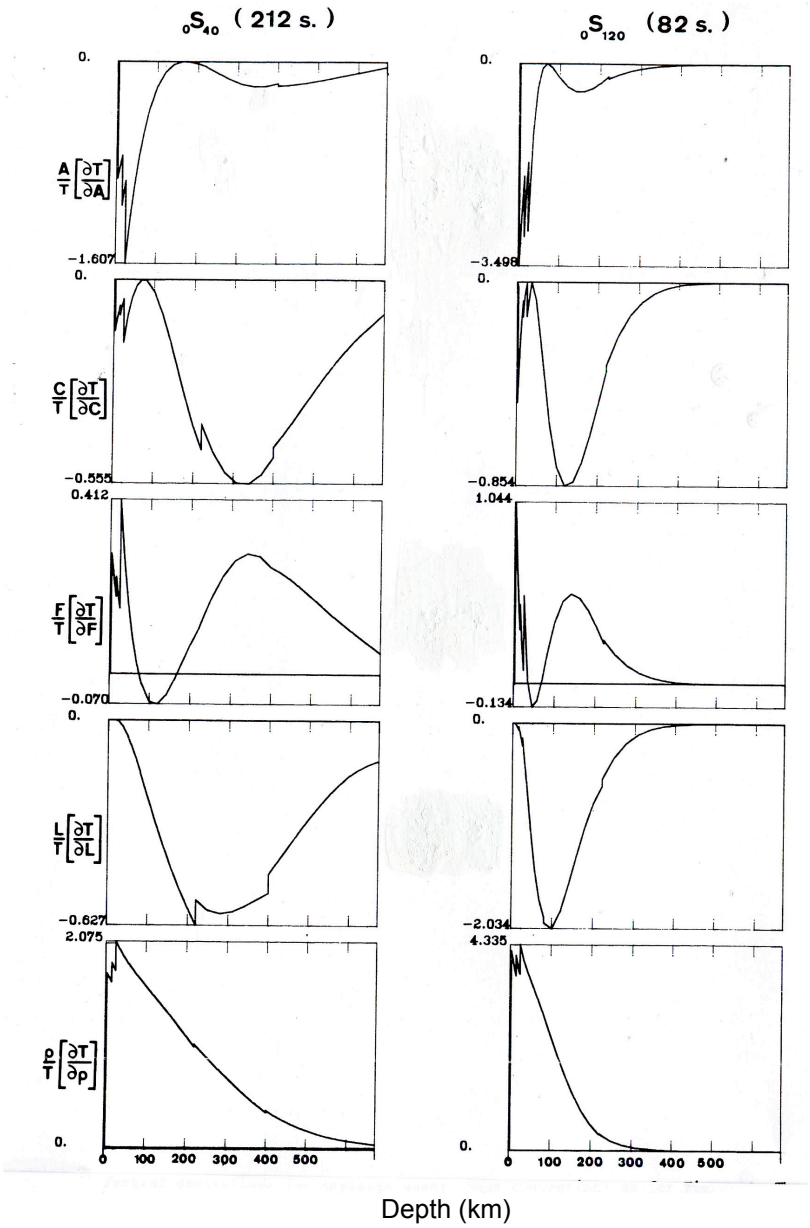

Figure A3 : kernels for Rayleigh waves. Same conventinos as for figure A1 in the same depth range. The partial derivative with respect to N has not been plotted since its amplitude is very small for fundamental modes. Note that 3 partials contribute to the 2Y-azimuthal terms , A-partial for B_c, B_s, F-partial for H_c, H_s and the largest one L-partial for G_c,G_s.